

---

---

SPECTROSCOPY OF GATE-TUNABLE  
THIN FILMS OF TUNGSTEN-DISELENIDE

---

SPEKTROSKOPIE LADUNGSDURCHSTIMMBARER  
DÜNNER SCHICHTEN AUS WOLFRAM-DISELENID

---

MASTER'S THESIS

By

JONATHAN FÖRSTE

SUPERVISED BY

PROF. DR. ALEXANDER HÖGELE

FACULTY OF PHYSICS – NANO-PHOTONICS GROUP

*LUDWIG-MAXIMILIAN-UNIVERSITÄT  
MÜNCHEN*

JUNE 8, 2018



## ABSTRACT

Two dimensional semiconductors made of transition metal dichalcogenides have attracted a lot of interest because of their unique optical and electrical properties like a direct band gap, strong spin-orbit coupling, valley polarization and a high exciton binding energy. Optical spectroscopy of these materials has however been limited by inhomogeneous broadening of spectral lines related to charge defects in the dielectric environment. Additionally, their varying degrees of intrinsic unintentional doping have made comprehensive studies of the reflection and photoluminescence impossible without external control over the density of free charge carriers. Both of these issues have been tackled during the course of this master's thesis. Using high quality hexagonal boron nitride as a substrate results in narrow linewidth photoluminescence spectra and the electric contacting to a lithographicly written gold-structure gives rise to gate-tunability. Confocal spectroscopy of a mono- and bilayer of tungsten diselenide both in the neutral and negative regime at different magnetic fields helps to classify previously misunderstood features.

---

Die besonderen optischen und elektronischen Eigenschaften zweidimensionaler Halbleiter aus einzelnen Schichten von Übergangsmetall-dichalcogeniden machen diese Materialien zu interessanten Forschungsobjekten. Die Kombination aus einer direkten Bandlücke im sichtbaren Bereich sowie einer starke Spin-Bahn-Kopplung, Valley-Polarisation und einer hohen Exziton Bindungsenergie ist einzigartig. Allerdings wird die Untersuchung dieser Systeme mittels optischer Spektroskopie durch Ladungsdefekte in der dielektrischen Umgebung erschwert, da Spektrallinien dadurch inhomogen verbreitert werden. Auch die intrinsische Dotierung, die von Probe zu Probe variieren kann, macht ein vollständiges Verständnis des Spektrums ohne externe Kontrolle der Ladungsdichte unmöglich. In dieser Arbeit werden diese beiden Aspekte aufgegriffen: Um eine defektfreie dielektrische Umgebung zu schaffen, werden die Proben in hexagonales Boronitrid eingebettet und mit lithographischen Goldstrukturen kontaktiert um die Ladungsdichte durch den Feldeffekt zu steuern. In konfokaler Spektroskopie wird das neutrale und negativ geladene Spektrum einer Mono- und Bilage aus Wolframdiselenid untersucht und das Verhalten der Spektrallinien im Magnetfeld beobachtet, um bisher unverstandene Linien zu klassifizieren.



# CONTENTS

1	INTRODUCTION	7
2	PHYSICAL PROPERTIES OF THIN FILM TRANSITION METAL DICHALCOGENIDES	9
2.1	Crystal structure and symmetries	9
2.2	Excitons in TMDC monolayers	10
2.3	Optical spectrum of wse <sub>2</sub> monolayers	12
2.4	The valley zeeman effect	13
2.5	Bilayer wse <sub>2</sub>	15
3	FABRICATION OF FIELD EFFECT STRUCTURES	17
3.1	Mechanical exfoliation	17
3.2	Layer number	18
3.3	Hexagonal boron nitride	19
3.4	Electrode fabrication	20
3.4.1	Top gate electrode	20
3.4.2	Back gate electrodes	21
3.5	Hot pick-up and transfer	22
3.6	Annealing	25
3.7	Electrical characterization	26
4	SPECTROSCOPY OF A WSE <sub>2</sub> GATE DEVICE	29
4.1	Optical setup	29
4.2	WSe <sub>2</sub> spectrum at different doping levels	32
4.2.1	Photoluminescence spectrum	32
4.2.2	Reflection spectrum	34
4.3	Modelling peak shapes	34
4.4	Measuring the valley zeeman effect	36
4.5	Comparison to bilayer wse <sub>2</sub>	40
5	SUMMARY & OUTLOOK	45



# 1 INTRODUCTION

Ever since Andre Geim and Konstantin Novoselov were awarded the Nobel Prize for their groundbreaking work on graphene, two-dimensional (2D) materials have become a centerpiece of condensed matter physics [1]. After graphene, hundreds of other 2D materials were predicted, including transition metal dichalcogenides (TMDCS). These 2D-semiconductors have attracted a lot of attention recently because of their unique valley physics, using the momentum of charge carriers as a pseudo-spin degree of freedom, that can be optically addressed [2]. The potential applications have created a hype around TMDC monolayers, that led to important milestones in the new field of “valleytronics”. For example the valley hall effect [3] that is analogous to the spin hall effect and results a valley-polarized drift perpendicular to a current, when the sample is illuminated with circular polarized light. Only recently the manipulation of the valley-index of excitons with femto-second light pulses was shown [4]. This could potentially allow optoelectronic computations, much faster than classical silicon-based information processing. But TMDC monolayers have gained attention not only because of their potential applications, but because the nature of these materials offers a unique model system to study physics in two dimensions.

On the spectroscopy side, this is mainly due to the special properties of optically excited excitons in TMDC monolayers. The confinement to two dimensions enables exciton formation well above room temperature and offers interesting applications as well as a system to study few- and many-body physics [5]. Point defects can lead to formation of quantum dots, that have shown characteristics of single-photon emitters [6]. The high absorption efficiency of their direct band gap enables strong coupling and the creation of exciton polaritons—bosonic superpositions of excitons and photons [7, 8].

The physical processes governing their light-matter interaction have yet to be understood completely [9]. The optical spectrum of TMDCS exhibits many features, whose identification is necessary to get an understanding of the involved physical processes and to pave the way for future applications.

While the spectrum is governed by the formation and recombination of excitons, especially tungsten-based TMDCS show a rich ensemble of peaks, whose origin has so far been elusive. The focus of this thesis lies primarily on the material WSe<sub>2</sub>. Spectroscopic analysis reveals signatures of both direct and indirect semiconductors. Direct excitons are known from other direct band gap semiconductor so are trions—excitons in a bound state with an additional free charge carrier. However, they also show features of so called momentum-indirect excitons that have net momentum and can only decay via phonon sidebands. They are associated with and indirect band gap.

One key to advance the research on TMDCS is sample quality. Spectral features can vary greatly from sample to sample, that can exhibit different levels of intrinsic unintentional doping as well as strain and contamination from the fabrication process. Meaningful spectro-

## *1 Introduction*

scopic studies are therefore tethered to the fabrication of high quality samples, that show a “pure” spectrum, including spectral lines that show little inhomogeneous broadening, no defect driven features and are compensated for unintentional doping. A step towards this goal can be achieved by suspending TMDCs in hexagonal boron nitride which offers an optimal dielectric environment to observe spectral lines close to the homogeneous linewidth [10, 11]. To compensate for intrinsic doping, samples have to be gate tuned with an applied voltage, that alters the charge carrier density inside the flake.

The goal of this thesis was to establish a process to fabricate samples in this manner. It utilizes the well established method of mechanical exfoliation for the production of TMDC mono- and bilayer samples and hBN substrate and capping layer. Using the novel fabrication technique of “hot pick-up and stamping” hBN-TMDC heterostructures are built and contacted to gold structures, that are fabricated with contact lithography. This enables photoluminescence (PL) and differential reflection measurements that demonstrate the increased quality and gate-tunability.

The complete fabrication of a sample that can be used in experiment can now be completed in around three days. Of the samples created for this thesis, one combined mono- and bilayer and an additional bilayer sample of tungsten-diselenide showed both narrow lines of between 2–7 meV and are gate-tunable between neutrality and a negative doping regime. This resolution was sufficient to resolve the exchange splitting of 5.2 meV for the trion [12], that only manifests in the charged regime. It distinguishes the trion from the energetically close spectral line in the neutral spectrum, that is associated with acoustic phonon sidebands of momentum-indirect excitons with an electron from the  $Q$ -valley and a hole from the  $K$ -valley. In magnetic field this peak has a  $g$ -factor of 11.5 which is different higher than that of the trion, which was measured both in PL and reflection. In the bilayer the spectral line associated with the  $QK$ -indirect exciton shows a similar  $g$ -factor of 12.1 that suggests a relation between both features.

The thesis is divided into three sections. The first part summarizes the physical properties of TMDCs that are relevant for optical studies. Then the fabrication and characterization of hBN-encapsulated samples is described in detail, followed by experimental analysis of the reflection and PL spectrum of WSe<sub>2</sub> mono- and bilayers for different charge densities and magnetic fields.

## 2 PHYSICAL PROPERTIES OF THIN FILM TRANSITION METAL DICHALCOGENIDES

### 2.1 CRYSTAL STRUCTURE AND SYMMETRIES

Transition metal dichalcogenides (TMDCS) belong to a class of materials that consist of large covalently bound sheets, that are held together by weak van-der-Waals forces. These so-called layered materials have gotten more attention since it has been shown, that individual monoatomic layers of them have unique properties, that are very different from the bulk material. The most prominent member of this group is graphene. Graphenes band structure shows what is called "dirac cones". This means that conduction and valence band touch at the  $K$  point at the edge of the Brilloin zone, with the Fermi level separating the two. The electronic dispersion relation in the vicinity of these "Dirac points" is linear. As a result charge carriers like electrons effectively behave like massless fermions, analogously to the linear dispersion of photons. This among other things causes very high electron mobility and conductivity. TMDCS on the other hand are semiconductors and have long been known to have an indirect band gap. However, only since the discovery of graphene their properties in the limit of one atomic sheet—the monolayer—came into focus.

Crystals of TMDCS consist of a tri-atomic base of one transition metal atom like tungsten (W) or molybdenum (Mo) and two chalcogen atoms like sulfur (S), selenium (Se) or tellurium (Te). In nature these compounds can be found in lateral arrangement—a TMDC monolayer (see figure 2.1 A). TMDS can exist in different metastable phases, that have a different crystal structure as well as different electronic properties [14]. The stable semiconducting phase is called 2H. In this configuration every transition-metal atom has six neighboring chalcogen atoms and forms a trigonal prismatic unit-cell, with the transition-metal in the center as depicted in figure 2.1 B. A TMDC monolayer exhibits a  $D_{3h}^1$ -symmetry. The unit-cell is invariant under 3-fold rotation as well as in-plane reflection. In the top-view (see figure 2.1 C) this looks similar to the hexagonal lattice structure of graphene, but with the key difference of a broken inversion symmetry. When the unit-cell is inverted with the transition metal atom as its inversion center, the chalcogen atoms wind up in empty locations as with any possible inversion point.

This has two important consequences, regarding the electronic band structure. As in graphene, the reciprocal lattice is hexagonal. At the  $K$  points however, instead of the characteristic dirac cone, monolayer TMDCS form a direct band gap in the visible range. Because of inversion symmetry breaking the degeneracy of the  $K$  points is lifted. The two different  $K$  and  $K'$  points that are identical in graphene are distinguishable in TMDCS and exhibit optical selection rules, coupling the valleys to light with opposite helicity. This circular dichroism gives rise to a new pseudo-spin degree of freedom—the "valley index". Analogous to electronics and spintronics, the term "valleytronics" has been coined to describe possible information processing by

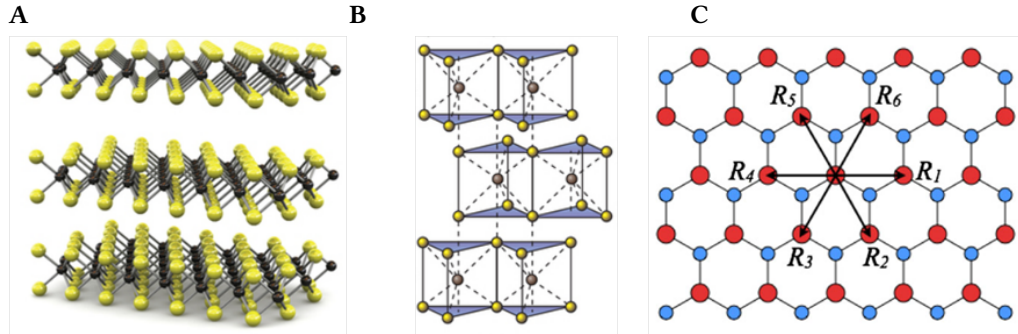


Figure 2.1: Crystal structure of TMDCs : **A** TMDCs are composed of large sheets of transition metal atoms sandwiched in between chalcogenite atoms. Individual sheets are bound by strong in-plane covalent bonds and are being held together out-of-plane only by weak van-der-Waals forces. **B** In the  $z\text{H}$  phase, the unit cell of TMDCs has a triagonal prismatic shape with the transition metal in the center, between two triangles of chalcogenite atoms. **C** Viewed from the top, TMDCs show a hexagonal lattice structure. However, because of the structure of the unit cell, the inversion symmetry is broken. Graphics from [2, 13]

manipulating this property [2, 13].

The valence and conduction bands of TMDCs are formed by the hybridization of the  $d$ -orbitals of the transition metal with the  $p$ -orbitals of its six neighboring chalcogen atoms. More precisely, the first four conduction bands and the seven first valence bands are dominated by the five  $5d$  ( $4d$ ) and  $4p$  ( $3p$ ) orbitals of W (Mo) and Se (S) respectively, carrying 93% of the total orbital weight [15, 16]. At the  $K$  and  $K'$  points the valence band is formed mainly by the  $d_{x^2-y^2}$  and  $d_{xy}$  orbitals of the metal atom, that leads to large spin-orbit coupling that splits the valence bands by more than 150 meV [17]. This energy is large enough to suppress any transition between the two valence subbands even at room temperature. Because of time-reversal symmetry, the splitting is reversed in the  $K'$  valley. With regards to optical transitions this results in tight locking of spin and valley degree of freedom. The conduction band—formed by the  $d_{z^2}$  orbital of the metal with some contribution from  $p_x$  and  $p_y$  of the chalcogen—exhibits much weaker but finite spin-orbit splitting, that leads to two distinct optical transitions  $X$  and  $D$ , that will be explained later on.

## 2.2 EXCITONS IN TMDC MONOLAYERS

When electrons absorb photons of an energy higher than the band gap of a semiconductor, they gain enough energy to be elevated to the conduction band and are allowed to move freely throughout the crystal. Other electrons can hop to the vacancies making the holes just as free as excited electrons. They also effectively act like a positive charges, resulting in Coulomb forces between free electrons and holes. If this interaction is strong enough to overcome thermal exci-

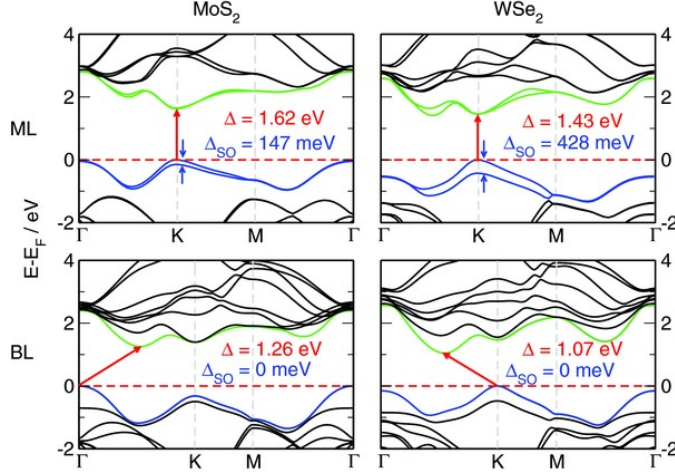


Figure 2.2: Band structure for  $\text{MoS}_2$  and  $\text{WSe}_2$  mono- and bilayers calculated for room temperature. In the limit of a single atomic layer TMDCs form a direct band gap at the K-point and the valence band is strongly split due to spin-orbit coupling. Graphic taken from [29].

tation, the two quasiparticles can enter a bound state, called “exciton”. In a bulk semiconductor electrons in between electron and hole weaken this interaction by screening the Coulomb interaction which results in a low exciton binding energy. The direct semiconductor GaAs for example exhibits an exciton binding energy of just 4.2 meV [18]. Doing a rough calculation with  $T = E_{\text{binding}} / k_B$  this corresponds to a temperature of 48 K, limiting exciton formation to temperatures well below that of liquid nitrogen. The geometry of TMDC monolayers however effectively reduces the screening effect. Because the movement of electrons and holes is confined to two dimensions, the electric field density in the material drops significantly and the strong Coulomb interaction between the free quasiparticles raises the exciton binding energy up to several hundred meV [5, 19, 20], corresponding to several thousand K in temperature. Therefore excitons can be excited at room temperature, which raises the possibility of exciton-based real-life applications. The Coulomb interaction results in an exciton Bohr radius of close to 1 nm and a very short lifetime in the order of picoseconds [21]. Hence, the recombination of excitons with emission of a photon is the most efficient optical decay channel and thus dominates the photoluminescence spectrum. The decay also happens faster than the so called valley lifetime—the timescale of coupling between the valleys—preserving the helicity in their emission once they decay. This is called “valley polarization”. The thinness of TMDC monolayers has additional implications. Since the electric dipole field of the exciton extends beyond the boundaries of the crystal, the dielectric environment has a big influence on the optical spectrum [22–24]. Impurities such as microscopic water droplets or dangling bonds of silicon oxide can induce localized potentials, broadening the linewidth of the photoluminescence (PL) features. This complicates spectroscopic studies. On the other hand, this high sensitivity could be used in quantum sensing applications to optically probe or visualize electric or magnetic proximity effects [25–28].

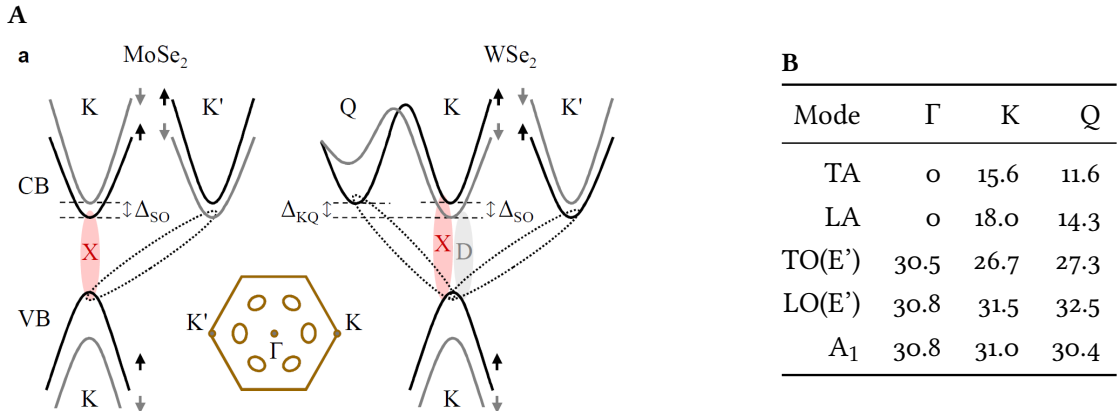


Figure 2.3: **A** Diagram of the band structure of  $\text{MoSe}_2$  and  $\text{WSe}_2$  [30]. In contrast to  $\text{MoSe}_2$  the spin-like bright transition (X) in  $\text{WSe}_2$  does not have the lowest energy. Because of spin-orbit coupling, the K valley with opposite spin is lower in energy, as well as the Q and K valley with parallel spin components. As a result the population of spin-forbidden and momentum-indirect excitons could be high enough to enable significant contributions to the PL spectrum by these states, whose radiative decay is less efficient. **B** The 3-atomic basis of TMDCs results in 3 acoustic and 6 optical phonon modes. Of these only 2 acoustic and 3 optical modes can couple to charge carriers. For QK and  $K'K$  indirect excitons—excitons with electrons in the Q/K'-valley and holes in K—phonons in the Q- and K-valley supply the right momentum to enable an optical transition and the formation of phonon sidebands. Their energies are theoretically calculated in [31] and given in meV.

### 2.3 OPTICAL SPECTRUM OF $\text{WSe}_2$ MONOLAYERS

As stated above, the optical spectrum of TMDCs both in reflection and PL is dominated by the decay of excitons. In Tungsten-diselenide ( $\text{WSe}_2$ ) the PL spectrum shows a rich ensemble of characteristic spectral features, that so far have not been identified unambiguously.

For hBN encapsulated  $\text{WSe}_2$  the main exciton resonance (X) is located at around 1.72 eV, but the precise value can shift several meV, mainly because of strain [32]. This resonance corresponds to the creation and annihilation of an exciton in the K valley with electron and hole having a parallel spin component. The corresponding exciton with antiparallel spins is often called the dark state as its “spin-forbidden” (D). For symmetry reasons® its radiative decay is only allowed in-plane and spin-orbit coupling puts the state about 40 meV lower than the bright exciton [33]. The PL from these excitons can be collected from the side or with a high numeric aperture objective, that catches light not directly emitted out-of-plane [34, 35]. In the presence of free charges—either holes or electrons—excitons can interact with them to form triions that are associated with a redshift of 20-30 meV [12]. While these properties can be predicted by modeling the triion as a three-body quasi particle, its precise nature still remains under discussion. The most contrarian interpretation to the helium-like bound state

is a so-called fermi polaron. In a charged regime excitons behave like an impurity in a “sea” of electrons, forming the polaron quasi particle [36–38].

The spectrum of WSe<sub>2</sub> shows additional features, that have so far escaped thorough understanding. In light of strong sample-to-sample variation, they are commonly attributed to localized effects, like defect-induced quantum dots or local doping [39, 40], that create trapped excitons. Improved fabrication techniques like mechanical exfoliation and the usage of hBN as a substrate (see section 3) have enabled experimentalists to measure spectra with very little defects and narrow linewidths, that still show a rich class of reproducible features.

#### PHONON SIDEBANDS

These peaks can be identified as phonon side-bands of momentum-indirect excitons [30]. It has been shown, that in contrast to molybdenum-based TMDCs WSe<sub>2</sub> actually shows an indirect band gap [41, 42]. As can be seen in figure 2.3 A, the *Q*-valley lies energetically close to the *K*-valley and is believed to be located lower than the upper *K*-valley, that participates in the direct spin-like exciton transition. This could point to a high population of excitons composed of electrons in the *Q*-valley as well as in the lower lying spin-like *K'*-valley. While both these states are spin-allowed, momentum conservation prevents them from radiatively decaying in a single-photon process. Instead they can recombine with assistance of an additional phonon, carrying the inter-valley momentum. For momentum conservation to hold, the following equations have to be fulfilled for momentum-indirect excitons in the *Q*- or *K'*-valley respectively:

$$\vec{k}_K + (\vec{k}_K - \vec{k}_{Q/K'}) = \vec{k}_K + \vec{k}_{\text{photon}} + \vec{k}_{\text{phonon}} \quad (2.1)$$

$$\Rightarrow \vec{k}_{\text{phonon}} \stackrel{!}{=} \vec{k}_K - \vec{k}_{Q/K'} \quad (2.2)$$

with  $\vec{k}_X$  being a reciprocal lattice vector with momentum X. Because of the hexagonal structure of the Brilloin zone  $\vec{k}_K - \vec{k}_{K'}$  simply equals a phonon in *K* while  $\vec{k}_K - \vec{k}_Q$  is conveniently close to a phonon in the *Q*-valley. Crystal vibrations in TMDCs can have three acoustic and six optical modes, but only two acoustic and three optical modes can couple to charge carriers. This leaves a total of five possible phonon sidebands for both *Q*- and *K'*-indirect excitons, neglecting processes involving more than one phonon. Corresponding theoretically calculated energies can be found in 2.3 B [31].

Phonon sidebands appear as a peak redshifted by these energy values. For *K'*-indirect excitons the positions of the peaks can be inferred directly, since the energy splitting between the spin-like and spin-unlike exciton is known and both features can be measured. The *Q*-valley however has no direct decay channel. Therefore, its energy has to be deduced from its sidebands.

## 2.4 THE VALLEY ZEEMAN EFFECT

A splitting of spectral lines in presence of a magnetic field has been studied for over a hundred years and is called the Zeeman effect is named after the scientist first measuring it in the spectral lines of sodium. The shift of different energy levels in an atom is a result of the magnetic

moment of the state, caused by its orbital angular momentum and spin. Solid crystals are large ensembles of atoms that merge atomic orbitals to form the electronic band structure. Likewise, this band structure can shift in a magnetic field just as orbitals of single atoms. The 2D-nature of TMDC monolayers and their broken degeneracy of the  $K$  and  $K'$  point gives rise to a new phenomenon called the “valley Zeeman effect”. It describes a shift in the band gap energy that is different for both valleys, leading to a splitting of spectral lines with different circular polarization [43, 44]. In the vicinity of the  $K$  point the band structure is dominated by large  $d$ -orbitals of the transition metal atoms. The hybridized  $d_{x^2-y^2} \pm id_{xy}$  orbitals give the valence band an orbital angular momentum along  $z$  of  $l_z = 2\hbar$  that leads to a magnetic dipole moment of  $\mu_{K,orb} = 2\mu_B$ . The conduction band is primarily formed by the  $d_{z^2}$ -orbital that has no out-of-plane angular momentum and therefore no magnetic moment along  $z$ . This leads to an asymmetric shift in the conduction and valence band and therefore to a shift of the band gap energy. The TMDC-geometry confines electron movement to the 2D plane, forcing the magnetic moment to either point upwards or downwards out of plane. This direction is exactly opposite at the  $K$  and  $K'$  points, shifting the valence band energy, and thus the band-gap in opposite directions. The total orbital magnetic moment at  $K$  has a value of  $\mu_{K,orb} = 2\mu_B$ . For the bright spin-like exciton transition this leads to a splitting between both helicities of  $\Delta_{K,K'} = 4\mu_B B_z$ . The prefactor in this equation is often called the  $g$ -factor and is given in units of the Bohr magneton  $\mu_B = e\hbar/2m_e$ . As it turns out, this first simple result is already in good agreement with experimental studies (see chapter 4). However, the main reason for this are that other contributions are small or cancel each other out, which is not generally the case. The main additional contributions are the spin of electron and hole and their respective effective masses. This leads to the following formula:

$$\Delta_B = g\mu_B B_z = 2\mu_B B_z \left[ (\tau_{e,orb} - \tau_{h,orb}) + g_e(S_e - S_h) + \left( \tau_e \frac{m_0}{m_e} - \tau_h \frac{m_0}{m_h} \right) \right] \quad (2.3)$$

The first part of this equation belongs to the angular momentum of the orbitals forming the band structure. In the conduction band this value is  $\tau_{e,orb} = \pm 2$  for  $Q/Q'$  while it vanishes for  $K/K'$ . Only the  $K/K'$  valleys are involved in the valence band and as discussed above, their contribution is  $\tau_{h,orb} = \pm 2$ . The second term in (2.3) corresponds to the spin component of electron and hole. The spin of each particle has a value of  $S = \pm 1/2$  which is multiplied by the single-electron  $g$ -factor of  $g_e = 2$ . The last term represents the correction from the quasi-particle effective masses with  $\tau_{e/h} = \pm 1$  representing the opposite direction of the magnetic moment in  $K/K'$  or  $Q/Q'$ .

In the spin-like direct exciton  $X$ , the observed  $g$ -factor of  $g_X = 4$  mostly stems from the orbital angular momentum. Parallel spin components cancel each other and the difference in the effective mass term is only minor. For the spin-unlike exciton  $D$ —all else being equal—the spins of electron and hole point in opposite directions. Neglecting the mass term, this yields a  $g$ -factor of  $g_D = 8$ . Predicting the  $g$ -factor for momentum-indirect excitons is more challenging though, because the difference in effective mass plays a more important role when electron and hole are coming from different valleys. Calculating the effective mass at a point in  $k$ -space can be done using a variety of theoretical approaches as done for example in [45] for

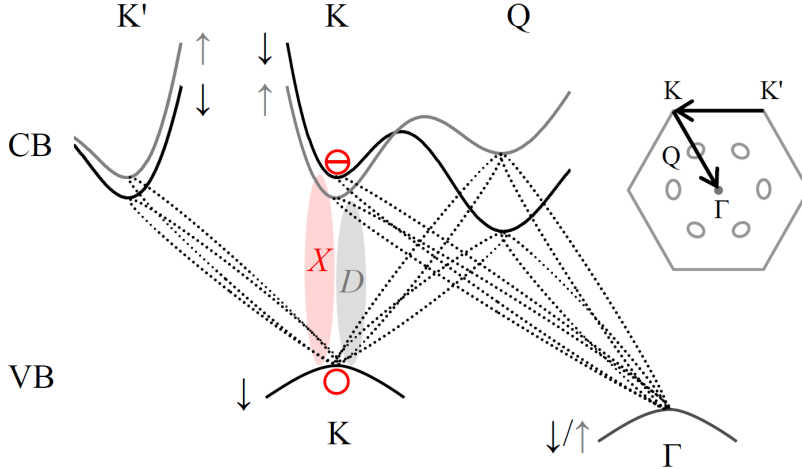


Figure 2.4: Bandstructure of bilayer WSe<sub>2</sub> [46]. With respect to the monolayer the Q valley in the conduction band drops significantly to form an indirect band gap with the K valley. Additionally, the  $\Gamma$  valley rises in the valence band, so that momentum-indirect excitations in  $QK$  and  $Q\Gamma$  become the energetically most favourable excitonic states.

the K-valley. Not including this term would result in a vanishing  $g$ -factor for the momentum-indirect exciton in  $Q$ . The data in section 4.4 strongly contradicts this simple calculation.

## 2.5 BILAYER WSe<sub>2</sub>

Even a single additional layer already fundamentally changes the properties of WSe<sub>2</sub>. Inversion symmetry is no longer broken and the Q valley drops below K in energy, yielding an indirect band gap [29]. Bilayer WSe<sub>2</sub> is of particular interest because spin and valley degree of freedom are also coupled to the layer pseudospin, the location **noch ersetzen**s of the excited electron in one of the two layers of the sample [47].

While in a bilayer the K valley in the valence band is still at the highest energy, the  $\Gamma$  valley is located only  $40 \pm 30$  meV below [48]. Because the Q valley lies lower than K in the conduction band the majority of PL of WSe<sub>2</sub> bilayers originates from the decay of momentum-indirect excitons. PL from the direct excitons involving electrons in K ( $X$  and  $D$ ) yield much less intensity.

Momentum-indirect states can be composed of holes in K and  $\Gamma$  for the valence band and of electrons in K and Q, with the K valley's spin orbit coupling, splitting it in  $K_{\uparrow}$  and  $K_{\downarrow}$ . In this notation  $K_{\uparrow}$  is spin-parallel to the valence band in K (see figure 2.3 A). In the same way Q is split into the lower lying  $Q_{\uparrow}$  and the energetically higher  $Q_{\downarrow}$ . In the following, omitting the arrows will correspond to spin-up or spin parallel to K in the valence band.

While combinations of all these valleys and their reversed counterparts could in principle contribute to the PL spectrum, it is expected that the lowest energy states will have the strongest population and their phonon sidebands should yield the highest intensity in PL. These are

## *2 Physical properties of thin film transition metal dichalcogenides*

excitons coupling  $Q$  in the conduction band and  $K$  and  $\Gamma$  in the valence band. The  $QK$  and  $Q\Gamma$  excitons are energetically close and it is not clear a-priori how they are ordered. According to measurements in [46] the latter one has the lower energy.

## 3 FABRICATION OF FIELD EFFECT STRUCTURES

The fabrication of gate tunable TMDC monolayer samples, that show narrow linewidth optical spectra is the centerpiece of this thesis. It is a condition for more accurate spectroscopic studies. This process is based on the work presented in [49]. Using the same mechanical exfoliation process in combination with standard contact lithography techniques and an advanced stamping procedure, it yields a fast and increasingly reliable process to build charge-tunable heterostructures of various 2D-materials.

### 3.1 MECHANICAL EXFOLIATION

Thin films of TMDCs, like many nanomaterials, can be fabricated using a top-down or bottom-up approach. The bottom-up method for TMDCs is to grow single layers via chemical-vapor deposition (CVD) [50]. Because of its scalability CVD is the leading candidate for an industrial fabrication pipeline. However, the top-down approach of mechanical exfoliation has become the first choice for a lot of projects to build high quality model systems, that can be used to study physics in low dimensions [51]. So far exfoliated thin TMDC samples show a superior crystal quality whereas CVD-grown monolayers exhibit a higher amount of mechanical and chemical impurities. Mechanical exfoliation also works hand in hand with dry transfer methods to build van-der-Waals heterostructures (See section 3.5).

The mechanical exfoliation process—often referred to as the “scotch tape method”—leverages the fact, that the van-der-Waals forces between adjacent layers in TMDCs are much weaker than the lateral covalent bonds. They are weak enough, that they can be easily broken apart by adhesive tape. The starting point is a single bulk crystal of TMDC-material, that can be produced either naturally or synthetically with high purity (bulk material for this thesis was supplied by hq-graphene). By bringing a stripe of adhesive tape in contact with the crystal, a small amount can be peeled off. With a second stripe, that is pressed on the first one, the process is repeated multiple times. Each time the fresh tape is peeled off its parent, the strong adhesion between tape and TMDC breaks the thin flakes further apart. Since the adhesive tape sticks much better to the material than the layers to each other a clean interface is ensured. Three to four repetitions are optimal to produce monolayers of a useful size. The chance to encounter bilayers is even higher. More repetitions increase the chance to find a larger number of thin flakes but heighten the risk of the fragile films to break to smaller pieces, which complicates processing the flakes later on and build larger devices.

To prepare monolayer flakes for the assembly of more complex devices, they first have to be transferred onto a suitable substrate. A standard substrate is silicon with a layer of thermal oxide that in our case is between 50 and 90 nm thick. Before wafers of this material are brought in contact with the exfoliation tapes they are cleaned both in acetone and isopropanol before being exposed to oxygen plasma for 180 seconds. This ensures a clean surface and maximizes

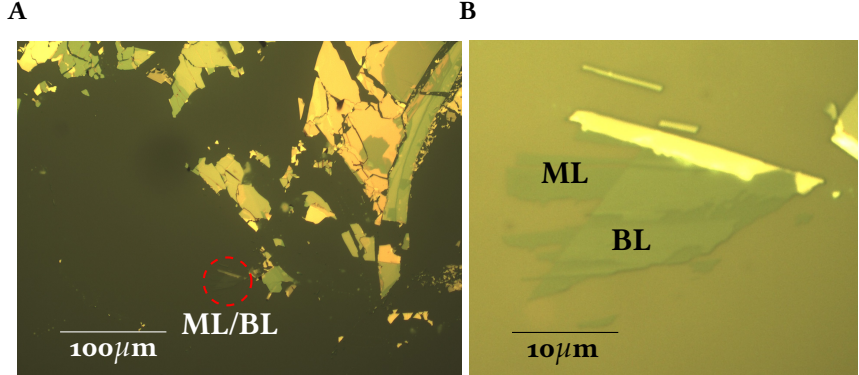


Figure 3.1: **A** During the exfoliation process a lot of flakes of different size and thickness are scattered over the substrate. Interesting specimen have to be searched for by hand. **B** Flake consting of mono- and bilayer regions that can be identified by their optical contrast.

the material that sticks to the wafer [52]. To release the tape, the substrate is heated to 85°C and kept at that temperature for at least 2 minutes. After cooling down the tape can be peeled off and the wafer is inspected for with an optical microscope. As seen in figure 3.1, this process yields a large number of flakes with different sizes and thicknesses on the substrate. It is likely to find at least one suitable monolayer sample on a typical Si-substrate (10 mm by 10 mm).

### 3.2 LAYER NUMBER

Under an optical microscope (Olympus® - BH2-UMA) mono- and bilayers can be identified using optical contrast and color as features to distinguish them from thicker films. It is possible to verify the layer number by these criteria alone using a camera and image analysis software [49]. However, this is much more reliable on transparent substrates, since the optical contrast is higher with an out-of-focus dark background. A reflective surface however enhances variations in the lighting conditions, making it harder to rely on absolute values of intensity. Suitable candidates where instead verified using photoluminescence (PL) imaging [28]. In TMDCs only monolayers show a direct band gap. Therefore even bilayers are much less efficient photonic emitters, showing almost an order of magnitude less PL -intensity. The sample is excited by a laser with a wavelength above the direct exciton resonance and only the PL is collected on the chip of a USB-camera. A detailed description of the optical setup can be found in 4.1. A sample measurement, comparing mono- and bilayer regions of WSe<sub>2</sub> in a standard microscope image with PL -imaging, can be seen in figure 3.2.

Other methods to identify monolayers include both PL and Raman spectroscopy [53–55]. However, to fit in a fast assembly process PL-imaging proved to be the best method to verify the layer number as well the overall quality of the sample.

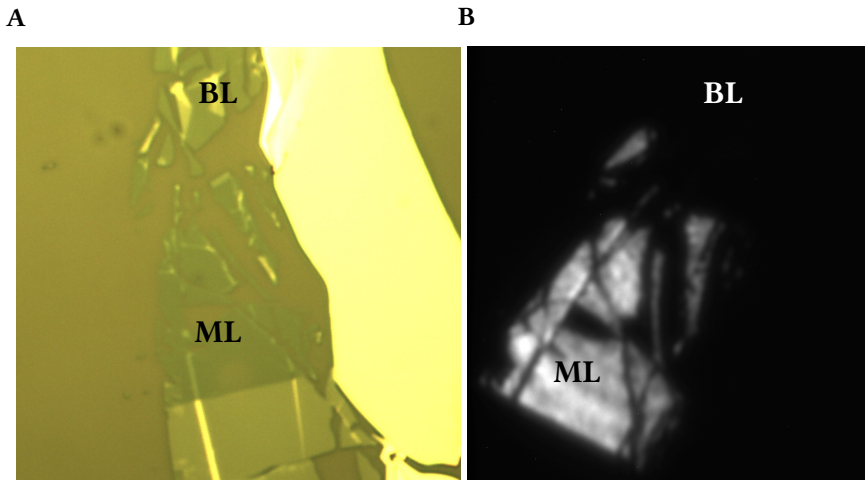


Figure 3.2: Comparison of mono- and bilayers of  $\text{WSe}_2$ . **A** The reflectance contrast of mono- and bilayers can be used to measure the layer number. The difference is however small enough to misidentify them under changing or inhomogeneous lighting conditions. **B** The PL -intensity of the monolayer is almost an order of magnitude higher than the bilayer and can therefore be identified very easily.

### 3.3 HEXAGONAL BORON NITRIDE

For spectroscopic studies of TMDCs the right substrate plays a crucial part. As discussed in section 2.2, the ultra-thin geometry of TMDC monolayers makes them very sensitive to the dielectric environment. To obtain a narrow linewidth of the spectral features both in reflection and PL spectroscopy, a suitable substrate has to fulfill some important specifications. A minimal surface roughness—ideally atomically flat—avoids local modulation of the band structure by strain. Also, the substrate has to be dielectrically calm. These criteria rule out traditional substrates such as Si and  $\text{SiO}_2$  whose dangling bonds cause localized charge defects, that introduce variations in the potential landscape of the TMDC sample and inhomogeneously broaden spectral lines. In recent years hexagonal boron nitride (hBN) has proven to be a superior choice to observe narrow linewidth spectra in TMDC's [56]. HBN, just like TMDCs, is a layered material but belongs to the class of 2D-isolators, with a large, indirect band gap in the uv-range [57]. Thin, flat layers of hBN can be mechanically exfoliated and achieve large, flat terraces. Few layers are sufficient to shield a TMDC sample from the underlying substrate. To achieve even narrower lines, it can be “sandwiched” between two flakes of flat hBN as was done with all samples contributing to this thesis. From the standpoint of fabrication hBN has another important property. The van-der-Waals forces at hBN-TMDC interfaces are stronger than between TMDCs and  $\text{SiO}_2$ . This is an important requirement for the hot pick-up assembly, discussed in section 3.5.

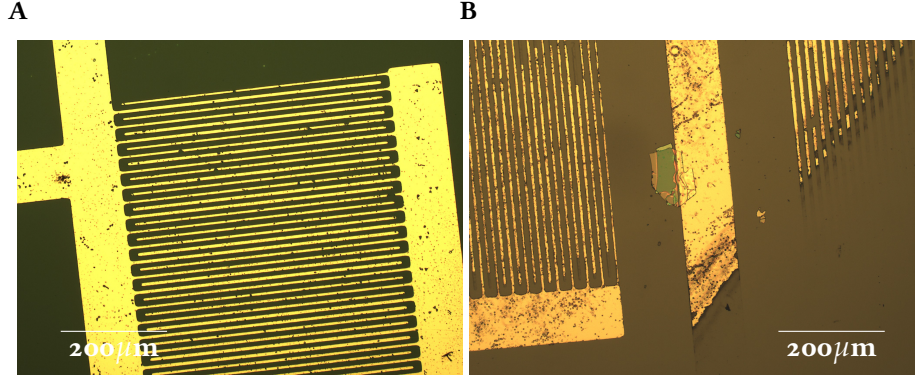


Figure 3.3: **A** Electrodes are written onto the substrate prior to the assembly of the hBN-TMDC heterostructure. A preused chromium mask of an interdigital structure is used for the gold pattern. **B** As long as the heterostructure is dropped in contact with a thick line of the gold pattern, minor defects in the electrode structure do not affect the functionality of the device.

### 3.4 ELECTRODE FABRICATION

A gate-tunable TMDC-device can be understood as simple capacitor. A gate voltage is applied between the TMDC-flake and the doped Si substrate—separated by a 50 nm layer of thermal  $\text{SiO}_2$ . As in a normal capacitor, this voltage shifts the Fermi energy and results in free charges entering the two sides. In case of TMDCs the voltage can also counteract intrinsic unintentional doping, by forcing free charges out the sample. Since TMDC monolayers experience a varying degree of this intrinsic doping, this configuration is important to tune the sample to neutrality.

#### 3.4.1 TOP GATE ELECTRODE

To contact microscopic structures like TMDC-monolayers, electrodes have to be fabricated using micro-lithography. TMD monolayers—either CVD-grown or exfoliated—are scattered on their substrates randomly. Therefore it is a common practice to fabricate electrodes directly on top of the sample via e-beam or laser lithography [58, 59]. Samples encapsulated in hBN usually feature one or more additional films of graphene that provide an ohmic contact outside the heterostructure. Since only one contact is sufficient for charge-tunability, the process can be simplified greatly. Instead of writing electrodes after transfer, contacts are fabricated on the bare substrate. The encapsulated hBN-TMDC-heterostructure can be contacted by dropping it on the edge of the gold structure. Most of the time, more TMDC-material than the monolayer is picked up during the transfer process. Because a TMDC-gold interface is conducting even at very low temperatures, these flakes provide suitable contacts, that do not have to be encapsulated in hBN, therefore replacing additional graphene electrodes. Gold patterns are fabricated in contact lithography using a chromium mask that is deposited on glass. Since the stack can be dropped at any point on the substrate, the shape of the gold structure is unimportant, as long as it is large and connected. Therefore not even a new lithographic mask had to be fabricated. Instead

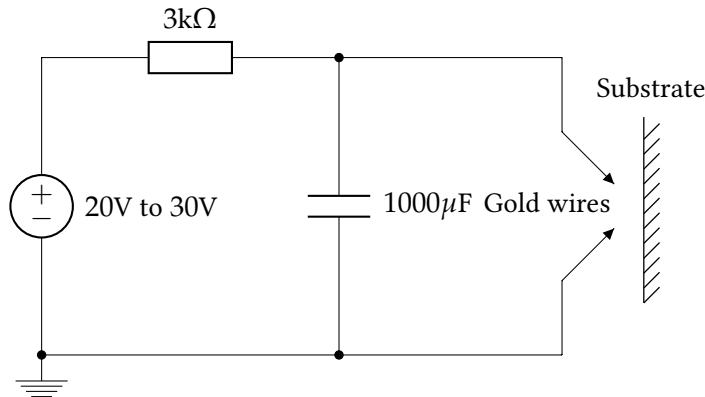


Figure 3.4: Circuit diagram for back gate fabrication: A capacitor is charged at 20V to 30V.

Two boron-doped gold wires are moved very closely to the silicon substrates. Once the distance between the wires and the substrate is low enough, an electric arc forms, discharging the capacitor through the substrate. Heat from the high current melts the tip of the gold wire locally doping the silicon and creating a gradient semiconductor/metal-interface.

a suitable mask was chosen from old pre-used structures. Even defects and deterioration of the masks only manifests aesthetically, rendering this process very robust and ideal for batch fabrication of gate-structures. The recipe starts with spin coating positive AZ 701 photoresist on a Si/SiO<sub>2</sub> wafer at 4000 rpm. Using a maskaligner, the wafer is brought in contact with the chromium mask before exposing it to uv-light for 18 seconds. After that, the pattern is developed using AZ 826 MIF developer, that washes out the exposed photoresist.

In the next step the sample is coated in an X-ray evaporation system. First, a 1–5 nm film of titanium is deposited on the substrate, that acts as a bonding agent. Subsequently a 50 nm film of gold is deposited on top. After removing the sample from the vacuum chamber the structures are finished in the so called “lift-off”. The substrate is simply suspended in a solvent like acetone, that dissolves residual photoresist, only leaving gold, deposited in the developed structures. To speed up the lift-off process the sample can be placed in an ultrasonic cleaner at a low power. The resulting structure can be seen in figure 3.3.

### 3.4.2 BACK GATE ELECTRODES

Silicon is a semiconductor. A simple contact with a metal wire therefore results in a Schottky barrier at low temperatures. To create an ohmic contact to the backgate, the semiconductor/metal interface is “smeared out” by diffusing boron doped gold into the substrate (see figure 3.4). This is achieved by applying a high voltage between two gold wires and bringing them close to the substrate. Because the Si-substrate has a higher conductivity than the ambient air, an arc discharge between the tips of the wires will preferably find its way through the substrate. When the arc forms the tips of the gold wire evaporate and penetrate the Si-substrate. This creates a gradual metal-semiconductor interface and avoids a Schottky barrier, leaving a small gold droplet on the surface that can be contacted to a thin wire using conducting paste.

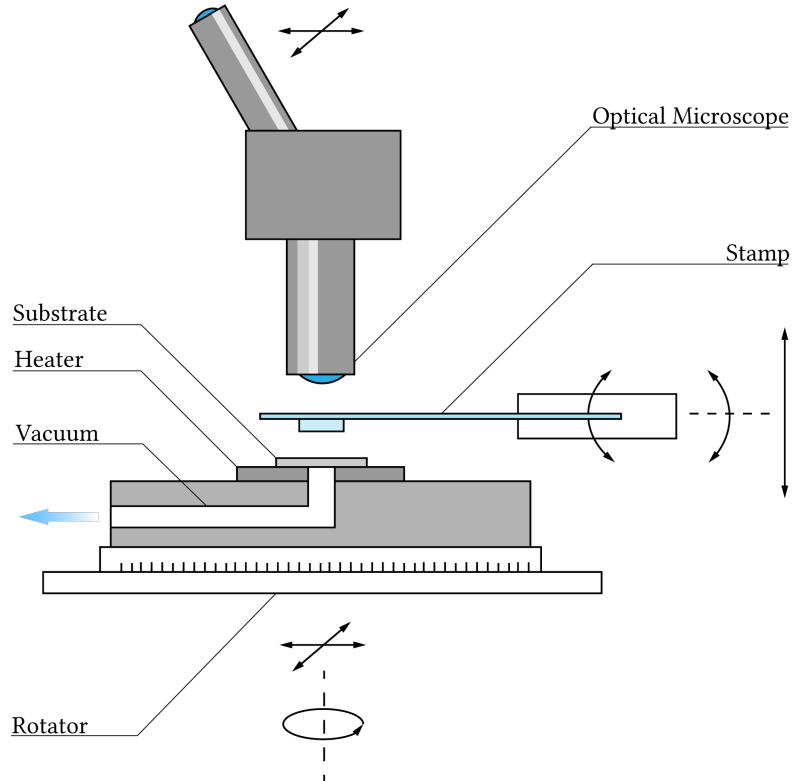


Figure 3.5: Setup for hot pick-up and stamping. The substrate is placed on a small, round **ceramic heater** with a 3mm hole in the center(Referenz Thorlabs), that is PID-controlled and can reach temperatures up to 200°C. It is mounted airtight onto the massive sample holder, that is connected to a **vacuum pump** to hold the **substrate** in place. It is **fully rotatable** and can be moved in plane. The **PDMS/PPC stamp** is monted to a z-translator and can be tilted with respecto to both in-plane axes. The **optical microscope** can also be moved in-plane.

This process can be very violent to the sample. Gold droplets can splash over a large distance and evaporated gold can not only diffuse into the backgate but can also contaminate the SiO<sub>2</sub> surface, lowering the breakdown voltage significantly. Therefore this step in the fabrication process should be taken before assembling the TMDC-hBN heterostructure. This way, the substrate can be replaced in case of failure.

### 3.5 HOT PICK-UP AND TRANSFER

The mechanical exfoliation method is popular also for its synergy with dry transfer methods. CVD-grown TMDC-flakes are grown on suitable substrates and can be transferred to a target substrate using a variation of wet methods, that involve powerful solvents or a combination of solvents and polymer films to lift the grown flakes off their initial substrate [60]. The advantage of the exfoliation method is that flakes can be put on any substrate directly from the adhesive

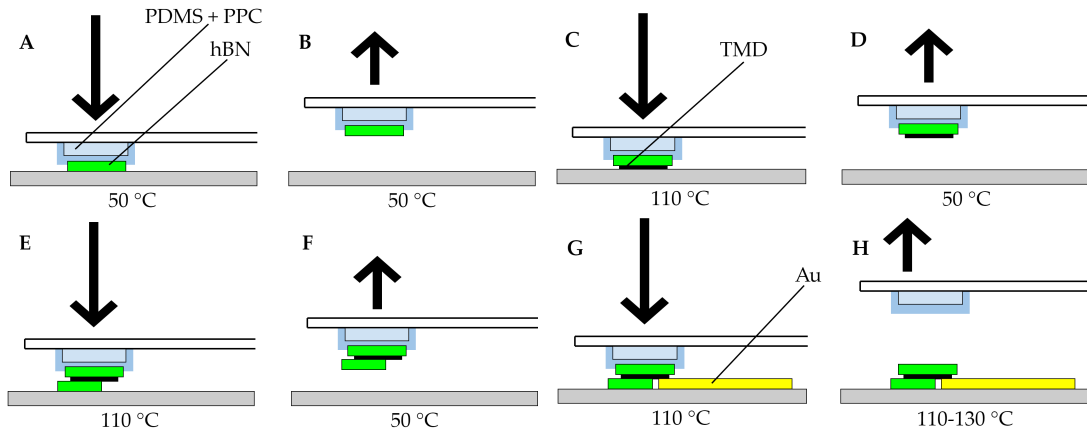


Figure 3.6: Stamping process: "Hot pick-up and stamping" is based on strong van-der-Waals forces between hBN and TMDCs as well as the control of adhesion between PPC and hBN using temperature. Flakes of hBN are picked up from a Si/SiO<sub>2</sub> substrate at 50 °C (A, B, D, F) and can be dropped at a temperature around 110 °C, when the PPC film on the PDMS block loses viscosity (C, E, G, H). Because thin TMDC flakes like mono- and bilayers adhere to hBN better than to their substrate, the pick-up is reliable—with around 10 samples, the pick-up has not failed so far—and arbitrarily high heterostructures can be built. To establish an electrical contact to a layer of the stack, part of it has to lay free, facing down. In this configuration the stack is simply dropped on the edge of the gold structure.

tape and do not encounter potentially damaging chemicals. This led to the invention of "viscoelastic stamping", where the TMDC-material is exfoliated on a substrate of viscoelastic polymer called polydimethylsiloxane (PDMS) [61]. This so called "stamp" can be brought in contact with the target substrate and peeled off carefully to drop down the flake at a desired position, opening up the possibility of producing carefully designed van-der-Waals heterostructures deterministically.

This method however can exclusively be used to drop TMDC flakes, exfoliated directly on the stamp. This is limiting in a number of ways, since exfoliation on a polymer like PDMS comes with unavoidable contamination of the sensitive samples, that only gets worse with every new layer stacked on top. Attempts to develop more flexible methods to pick up TMDCs and other 2D materials from clean substrates failed because van-der-Waals forces between the flake and a substrate like SiO<sub>2</sub> could not be reliably overcome with a viscoelastic stamp. That is until hBN was introduced as a more suitable substrate. It turns out, that van-der-Waals forces between hBN and TMDCs are high enough to remove them from SiO<sub>2</sub> deterministically while a range of polymers can be used that strongly adhere to hBN at an appropriate temperature.

This method is called "hot pick-up and stamping" [52, 62]. The stamp used in this process is a block of PDMS, mounted on a glass slide with transparent adhesive tape. The active polymer however is polypropylene carbonate (PPC), that is spin-coated onto the PDMS-block to form a thin, adhesive coating. PPC, as a polar polymer sticks best to other hydrophilic substances.

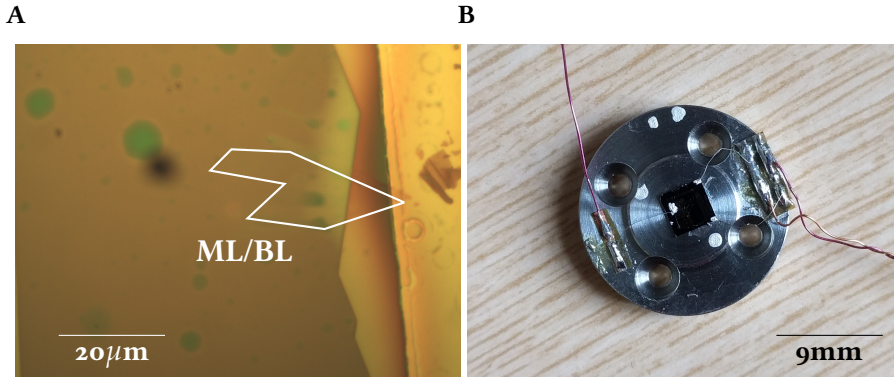


Figure 3.7: **A** Finished sample of both mono- and bilayer WSe<sub>2</sub>. Most of it is encapsulated between two flakes of hBN. To establish electrical contact part of the TMDC material has to be in mechanical contact with the gold structure which is seen on the right. **B** Finished sample mounted onto a chip-carrier made of titanium. The top-gate is contacted by gluing a thin wire to the gold structure on the surface with conductive silver paste. The backgate contacts are contacted in the same manner by gluing wires to the points where gold was deposited during the arc discharge. These thin wires are mounted on conducting pads on which thicker wires are soldered.

Therefore if the hydrophobic PDMS is coated with PPC without additional treatment it can peel off, when in contact with SiO<sub>2</sub>, especially at higher temperatures. However, the adhesion can be greatly enhanced by exposing PDMS to oxygen plasma [63]. Before spin-coating, all stamps are treated in a plasma-etching system (Gigaetch 3000) for 20 minutes, at 200 W of power.

The TMDC and hBN-flakes are exfoliated on a Si/SiO<sub>2</sub> substrate. To raise adhesion with the flakes, these substrates are treated in oxygen plasma as well (180 s at 200 W). The primary criteria for finding the right hBN-flakes is the flatness of its surface, so that the TMDC-flake can be encapsulated between two large terrasses without cracks or steps. To allow a fast fabrication process, this flatness is only judged with help of an optical microscope. More sophisticated methods like atomic force microscopy can be used to verify the flatness more accurately. This is however much more beneficial, if the thickness of the hBN plays an important role, for example when it is used in an optical microcavity [36].

The goal of the hot pick-up is now to use a hot-plate to control the van-der-Waals forces between hBN, TMDCs and the substrate to ensure adhesion between the parts of the heterostructure as well as to reduce contamination with water molecules from the ambient air.

After all precursors are prepared on Si/SiO<sub>2</sub> substrates, the actual pick-up and stamping process can be carried out. The fabrication setup can be seen in figure 3.5 and a the process in 3.6. The first step is the pick-up of the top hBN flake. At 50°C the van-der-Waals forces between hBN and PPC are already strong enough to lift the flake off the silicon substrate. Bringing flake and PPC in contact at a higher temperature can help as well, because this reduces the polymers viscosity. When cooling down to 40°C to 50°C afterwards, it becomes more rigid again and sticks to the hBN more easily. In the next step the hBN is dropped on the TMDC-flake. At a higher

temperature of  $110^{\circ}\text{C}$  PPC becomes almost fluid and peels off hBN with ease. While the adhesion between thin TMDC flakes and hBN are strong enough to facilitate a pick-up also way below that temperature, heating the substrate during the drop helps to reduce the contamination with droplets of water. Since both TMDC and hBN flakes are prepared on clean wafers, humidity in the ambient air of the clean-room seems to be the biggest concern. Raising the temperature above the boiling point both minimizes the formation of actual droplets and also makes blisters of humid air and other contaminants at the hBN-TMDC interface more mobile. Dropping the stamp very slowly therefore helps to push these blisters out to the edge of the substrate [52]. The stack of TMDC and hBN can then be picked up again following the same procedure that was used for the bare hBN flake. By repeating both steps of pick-up and drop-down an arbitrary number of layers can be added to the heterostructure. In this case it is dropped down on the bottom hBN flake. To contact the TMDC flake to gold, it has to remain outside the hBN encapsulation. This part does not necessarily have to be a monolayer, but can also be any form of TMDC , that is in contact with it so charges can be transported. The hBN on the other hand is elastic enough so that thicker material does not affect the encapsulation of mono- or bilayer regions.

The last step is to transfer the whole stack to its final position in contact with the electrodes. This is accomplished by repeating the pick-up process once again and dropping the stack in contact with the gold structure.

Despite the strong plasma treatment of the PDMS-stamp in some cases the PPC can peel off during the drop down part of the transfer due to high heat as the polymer becomes ever more liquid. In this case the sample can be carefully treated in a bath of acetone, which dissolves the polymer rapidly. The sample should stay in the bath for around one minute without any mechanical stress. Afterwards it has to be cleaned in isopropanole and blown dry with nitrogen gas. The finished sample can be seen in figure 3.7.

### 3.6 ANNEALING

While the hot pick-up should in theory ensure a hBN-TMDC interface free of contamination, especially contamination due to humidity in the ambient air can remain between the layers and seriously lower the quality of the sample. To remove this pollution, the sample can be annealed [64]. During annealing, the sample is placed in an annealing oven. While maintaining a high vacuum of  $10^{-3}$  mbar, the oven heats the sample to  $250^{\circ}\text{C}$  for three hours. The vacuum ensures that any volatile materials like water vapor dissipate, while the high temperature increases the mobility of water and eventual polymer contamination on the surface. While not all dirt completely evaporates, the annealing procedure results in the formation of tiny bubbles, so that most of the interface remains clean while all dirt packs at a few avoidable places. Other recipes, that use higher or lower temperatures or longer annealing times can work just as well. Water contamination from the ambient air is still the biggest concern, so even mild temperatures should have a clear advantage over not performing the annealing-step at all. More aggressive recipes, that work at higher temperatures or for longer times can be more effective regarding polymer contaminations that arise from contact to the stamp. If the sample had to be freed of the residual PPC layer with acetone, contamination with polymer molecules is possible. When this exposure can be avoided however, raising the temperature has a limited

advantage over milder annealing conditions, but raises also the risk of damaging the sample through temperature induced strain, that can potentially rip the TMDC flakes.

### 3.7 ELECTRICAL CHARACTERIZATION

To assess the quality of the gate structure, its breakdown voltage has to be determined. This is the voltage between top gate and back gate, at which the leakage current starts to rise exponentially by forming conducting channels through the dielectric, that are self-sustaining and lift the conductance permanently [65]. This breakdown voltage is complicated to predict, as it is a nonlinear effect mainly caused by faults in the  $\text{SiO}_2$  layer. Thus it does not only depend on the thickness of the dielectric but also on the area of the top gate, because the statistical chance of encountering a fault in the material and a conducting channel forming is higher the more area of the sample is covered with conducting material. Additionally the rather violent ohmic contacting of the backgate can also damage the dielectric and lower the breakdown voltage. Therefore each sample has to be classified before being used to tune the charge density in optical spectroscopy. The dielectric in samples used throughout this thesis had a thickness of 50 nm or 90 nm, corresponding to a predicted breakdown voltage of 47.5 V or 85.5 V respectively. To verify these values, the leakage currents have to be monitored while ramping up the voltage. Before breakdown these currents are of the order of 100 pA to 1 nA and can be measured using a lock-in amplifier. A diagram of the circuitry is drawn in figure 3.8. A constant voltage across the desired range of operation ( $\pm 30\text{V}$ ) is added to a small AC-voltage of small amplitude ( $U_0 = 10 \text{ mV}_{pp}, f = 77.1 \text{ Hz}$ ). The amplifier can monitor the real and imaginary part of the current. The real part is the resistive current, or leakage, that flows through the samples dielectric. The imaginary part is proportional to the capacity. By first performing the experiment with a gauge capacitance, the capacity of the sample can be measured with high precision. For the purpose of characterizing the dielectric however, the resistive current is the more interesting quantity. To find the breakdown voltage the DC-voltage is ramped until the leakage rises exponentially. At this voltage, the resistive current is still usually still below a few nA—small enough to not inflict permanent damage to the dielectric and marks a safe range of positive and negative voltages the device can be operated on during the experiment.

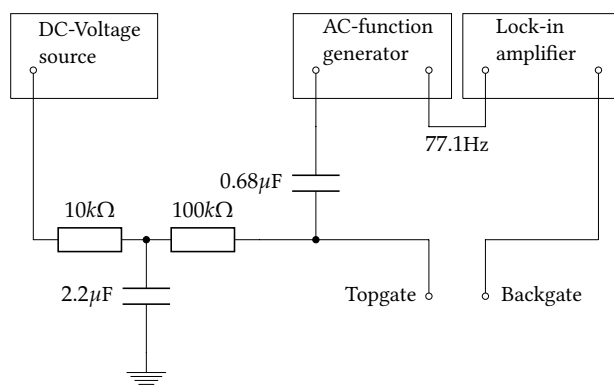


Figure 3.8: Diagram for the cv-measurement. Using a lock-in amplifier and a small AC voltage added to a DC voltage even very small resistive currents leaking through the samples dielectric can be measured. This way, the maximum gate voltage at the gate can be obtained, by ramping the DC voltage source until the resistive current starts to rise exponentially.



## 4 SPECTROSCOPY OF A WSe<sub>2</sub> GATE DEVICE

The fabrication techniques discussed in the last chapter yielded in promising samples of tungsten-diselenide (WSe<sub>2</sub>) mono- and bilayers. The results of spectroscopic measurements on these samples are presented in this chapter. Its quality will be assessed by fitting peak functions to the spectral lines to find their linewidth. The same procedures are used to track the peak positions both at different charge densities and different magnetic fields to find *g*-factors of the spectral lines to classify their behavior more precisely.

### 4.1 OPTICAL SETUP

The optical setup is a confocal microscope operated at cryogenic temperatures. This means that the sample is placed in the focal plane of a low temperature objective and instead of capturing a wide field image of the sample only the signal from the focal point is collected. With a high quality objective the spot is only limited by the fundamental diffraction limit, yielding high spatial resolution. The other advantage is the high ratio between excitation power and collected signal, which extends the limits on integration time and thus the signal to noise ratio. A diagram of the complete setup can be seen in figure 4.1. The excitation beam from a laser is guided to the so called excitation arm with a single mode optical fibre. It passes through a linear polarizer to define a polarization axis and is reflected to the objective by a beam-sampler. To analyze circular dichroism in the detected beam, it passes through a quarter waveplate and another linear polarizer before being coupled into another optical fibre, that is connected to a spectrometer. The sample is mounted on a piezo nanopositioner inside a cryostat or a container of liquid helium and connected to a voltage source, that can tune the charge density in the TMDC flake. A strong, homogeneous magnetic field along the *z*-axis of the sample can be supplied by a superconducting magnet.

For PL spectroscopy, the sample is excited by a laser beam with a narrow frequency profile and high power. The optimal parameters are determined by different factors. The optimal laser power depends on the observed features. At a very low power emission from quantum dots can be observed, that saturate and bleach at a higher intensity—this is desirable in this case, as the observed spectrum should be as representative as possible. If the power is too high though, non-linear effects such as the formation of bi-excitons can start to play a role and the exciton emission saturates. Even before that the spectral linewidth of some peaks can rise significantly with the power, lowering the resolution of the spectrum (see figure 4.2 A). Another problem of too high laser power is photoinduced doping, that counteracts the unintentional doping with an applied gate voltage [66, 67]. Therefore tuning to the negative regime only works for low excitation power. Even at low powers this beam has a much higher intensity, than the collected PL and has to be tuned to a higher frequency than the main exciton resonance, to obtain a complete spectrum without disturbance from the excitation beam. To avoid stray light inside

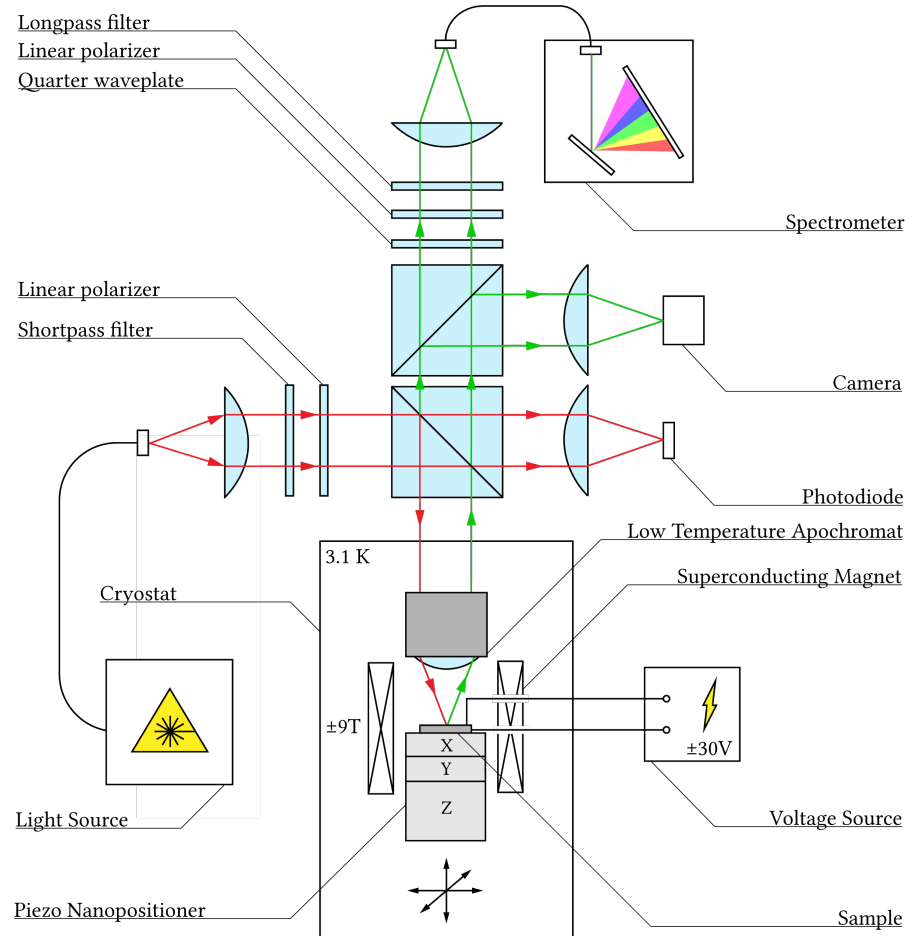


Figure 4.1: Optical setup for confocal spectroscopy: Light from a **laser**-source is guided to the setup in a single mode optical fiber and collimated. To cut off raman-modes, that are created in the fiber a **shortpass** filter is installed behind the collimator. A **linear polarizer** defines a polarization axis. A **beam-sampler** is reflecting the excitation beam into a **low temperature apochromat**, whose focus lies on the sample, with a spotsize of  $\sim 0.5\mu\text{m}$ . The sample is mounted on a **piezo nanopositioner**, that is placed inside a **cryostat** at a temperature of up to 3.1 K or in a container of liquid helium at 4.2 K. The cryostat is equipped with a **superconducting magnet** that can supply a homogeneous magnetic field up to 9 T. The sample electrodes are connected to a **voltage source** (Yokogawa) that supplies  $\pm 32\text{V}$ . The detection spot is identical with the excitation. The reflection or photoluminescence is collimated again in the objective and passes through a  $\sigma^-/\sigma^+$ -analyzer consisting of a **quarter waveplate** and a **linear polarizer**, before being focussed in the detection fibre that connects to a **spectrometer**. A **camera** can be used to monitor the spot and image the sample, if it is brought out of focus.

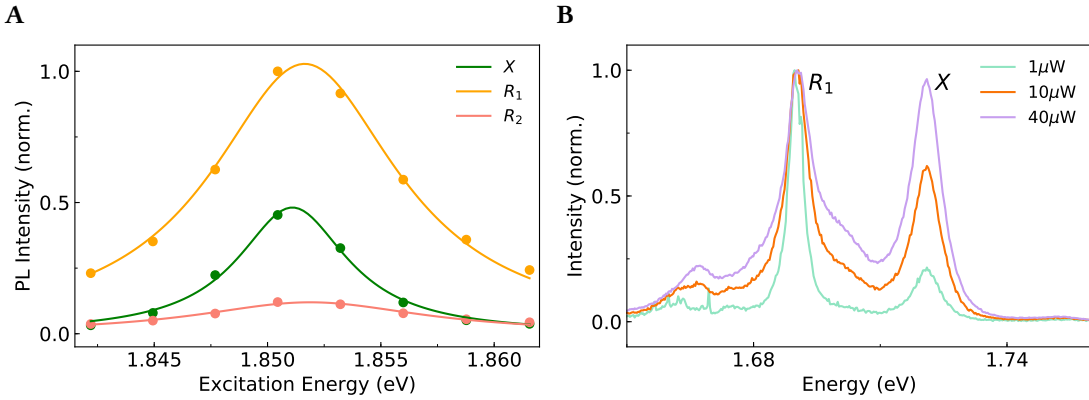


Figure 4.2: **A** Photoluminescence-excitation scan over the 2s resonance in WSe<sub>2</sub>. To observe the complete spectrum, excitons have to be excited off-resonance. To create excitons as efficient as possible an excited exciton state, the 2s state can be pumped, that lies about 30 nm or 150 meV above the main exciton resonance. In this sample all spectral lines are at maximum intensity when pumped at 1.851 meV or 669.3 nm. **B** A higher excitation power means shorter integration times and higher signal to noise ratio but also broadens the spectral lines. For the R<sub>1</sub> peak the linewidth rose from 4.3 to 12.0 meV between 1–40  $\mu$ W of excitation.

the spectrometer a longpass filter additionally blocks the laser before entering the detection fiber. A shortpass filter in the excitation arm blocks Raman modes of the optical fiber, a result from high excitation power, that can have frequencies overlapping with the PL of the sample. Pumping off-resonance however results in a very inefficient ratio between excitation power and collected PL. To still achieve a good signal-to-noise ratio, an excited state of the exciton—the 2s resonance—can be pumped (see figure 4.2 A). While this resonance is much weaker than the main exciton resonance tuning the excitation beam to the corresponding frequency still results in a signal five times more intense than while exciting off-resonance. The setup only has to be mildly altered to perform reflection spectroscopy. The sample is illuminated with a broad band white light source at a low power, therefore all color filters are omitted. Because the excitation laser generally has a non-uniform frequency profile it has to be filtered out to get the reflection signal from the WSe<sub>2</sub> flake. Additionally, because TMDC monolayers are not opaque the substrate can modulate the reflection signal as well, especially a transparent material like hBN, that can cause interference effects. This can be compensated for by recording a spectrum close to but not on the sample. During post-processing this background spectrum can be subtracted.

$$S_R = \frac{\Delta R}{R} = \frac{R_{\text{flake}} - R_{\text{background}}}{R_{\text{background}}} \quad (4.1)$$

The signal  $S_R$  is the difference of the Reflection signals of TMDC flake and background. The division by the background reflection is made to normalize the signal. The resulting reflection spectrum should show only features of the sample itself. When evaluating the data, one has to



Figure 4.3: Photoluminescence of monolayer WSe<sub>2</sub> at different doping levels. **A** Spectra in the neutral and negatively charged regime. The PL of the exciton (X) is clearly visible at the blue end of the spectrum. The replica peaks ( $R_1$ ,  $R_2$ ) correspond to acoustic phonon sidebands of Q- and  $K'$ -indirect excitons with low-intensity features to the red indicating optical sidebands. In a negatively charged regime, they vanish in favor of redshifted peaks, that correspond to the trion ( $X^-$ ) that is split by electron-electron exchange interaction, and its momentum indirect counterparts. While  $R_1^-$  fits the picture as an acoustic sideband of  $X^-$ ,  $R_2^-$  seems to be the charged spin-unlike dark state. **B** Spectral features in a gate-sweep. The plot can be divided into a neutral and charged regime below and above 5 V. This threshold is a signature of unintentional n-doping and varies across the sample.

bare in mind, that even slight differences in height like that of a mono or bilayer can potentially affect the interference pattern of the heterostructure and will show up on the supposedly pure reflection spectrum.

## 4.2 WSe<sub>2</sub> SPECTRUM AT DIFFERENT DOPING LEVELS

In all semiconductors the density of free charges through intentional or unintentional doping strongly influences its behaviour. TMD samples very often exhibit unintentional doping [68, 69]. Additionally, other defects of different nature leave marks in the optical spectrum [70, 71]. The discussion and interpretation of the spectrum thus becomes harder and highly speculative in samples prepared without control of the charge density. Gate-tunability therefore becomes a necessary tool to establish a ground truth for a neutral sample, but also to study the spectrum in charged environment intentionally.

### 4.2.1 PHOTOLUMINESCENCE SPECTRUM

The PL spectrum is pictured in figure 4.3 both in a neutral and charged regime. The sudden change in the spectrum at 5 V shows, that at this point on the sample, the TMDC-flake is negatively doped. As a result only the neutral and negative regime could be studied. The peak to

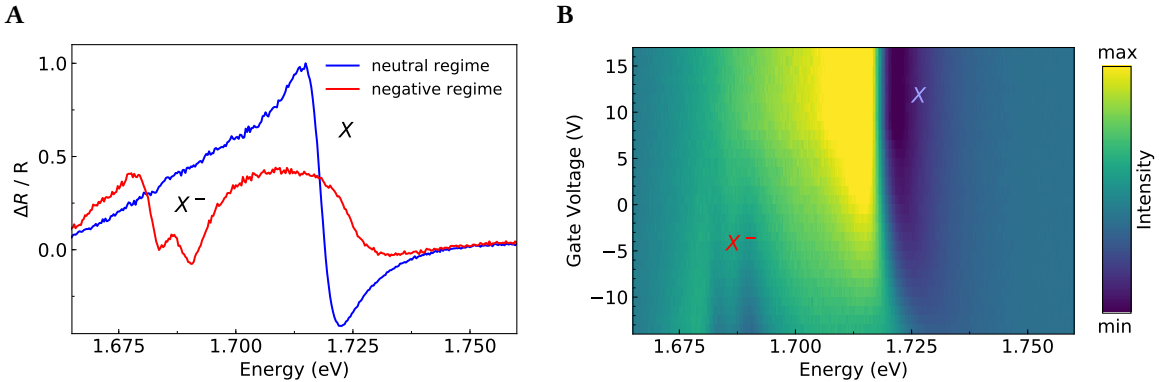


Figure 4.4: Reflection of monolayer WSe<sub>2</sub> at different doping levels. **A** The reflection spectrum of WSe<sub>2</sub> in a neutral and negatively charged regime. The neutral spectrum shows a strong response, corresponding to the main exciton resonance (X). The absorption of the exciton almost vanishes in the charged spectrum and a double dip appears, that corresponds to the trion resonance, resolving the typical exchange splitting (X<sup>-</sup>). **B** Reflection spectra at different voltages. The exciton absorption shows a similar response as in PL, however stretched to lower voltages. The absorption at the trion resonance can be resolved much better, than the corresponding peaks in PL.

the blue end of the spectrum belongs to the direct spin-like neutral exciton (X). This peak is well understood and can therefore be used to benchmark the spectral linewidth and the overall quality of the sample. With a linewidth of 6.8 meV the exciton is still above the intrinsic homogeneous linewidth which is reported to be below 2 meV [72, 73]. Inhomogeneous broadening can be mostly attributed to local changes in the potential landscape that can arise from defects, impurities as well as strain induced shifts in the band structure [32]. The diffraction limited spot of the objective is large enough to cover a large ensemble of slightly different contributions to the PL signal, that merge to a broad peak. Apart from the FWHM linewidth of the exciton peak, both a significant asymmetry parameter in the fit as well as a slight deviation from the lorentzian line-shape are indicators, that the feature has an considerable substructure and there is still room for improvement in terms of sample fabrication.

However, the linewidth-limited resolution of the present sample is good enough to distinguish the fine splitting of the trion peak in the charged regime (X<sup>-</sup>). When the gate voltage is tuned, the Fermi level is shifted. The negative regime is reached when the Fermi level rises above the lower K and K' valleys in the conduction band and free charge carriers enter the flake. Optically excited excitons can bind electrons from either of the two valleys resulting in two a-priori degenerate trion states, that differ energetically because of a difference in Coulomb exchange interaction [12]. The resulting splitting can be resolved in the present sample and has a value of 5.2 meV. The spectral difference to the exciton peak in the neutral regime gives an estimate of an additional trion binding energy. Taking into account the exchange splitting it has a value of 30.5 - 35.8 meV. Since the separation of the two trion peaks is quite low, the

linewidth estimates from the fit are only a rough estimate but are close to the neutral exciton at 5-7 meV.

The peaks to the red in both the neutral and charged spectra can be explained using the phonon sideband model described in 2.3. The  $Q$ -indirect exciton should lie above the direct spin-unlike state. Therefore it makes sense to identify the intense  $R_1$  peak with its acoustic sidebands, putting the  $Q$ -exciton roughly  $19 \pm 2$  meV below  $X$ . The optical sidebands coincide with a low intensity bump that fits the predicted energies. The direct spin-unlike exciton ( $D$ ) should be 40 meV to the red of  $X$ , but cannot be resolved clearly, possibly because  $R_1$  is broad and intense enough to merge with the weak PL of  $D$ . Its momentum-indirect counterpart in  $K'$  should have the same energy, thus we can estimate its phonon sidebands, which fit the strong  $R_2$  peak and the corresponding low-intensity feature to the red.

Assuming the nature of the phonon sidebands does not change fundamentally in a charged environment it is worth a try to treat the charged spectrum in a similar fashion. Analogous to the trion, the energy of the peaks should redshift upon interaction with free charge carriers. When shifting the  $Q$ -valley by the trion binding energy, it fits the two most intense replica peaks in the charged spectrum ( $R_1^-$ ,  $R_2^-$ ). However,  $R_2^-$  also matches  $D$  shifted by the trion binding energy. This could explain the relatively strong signal at this energy. The weak feature to the red could then charged acoustic replica of  $K'$ .

#### 4.2.2 REFLECTION SPECTRUM

The reflection spectrum offers a way to quantify a materials absorption. In TMDCs it can therefore offer a way to disentangle exciton resonances from states, that form by their non-radiative decay. These include the discussed phonon sidebands but also defect states and quantum dots, that have low absorption but brighten up trapped excitons [6]. The reflection spectrum therefore offers a more “pure” view on the direct exciton and the charged trion. The reflection spectrum can be seen in figure 4.4. The neutral spectrum shows a clear signature of the direct exciton resonance ( $X$ ). This spectral feature in an hBN encapsulated sample has the shape of a fano resonance, because of interference effects. The TMDC-hBN heterostructure acts as a microcavity and shows very high reflectivity at the resonance frequency [74]. Upon tuning the gate to negative voltages, the absorption and reflection at the exciton resonance is suppressed and the trion resonance forms ( $X^-$ ). Just like in PL this resonance exhibits a splitting due to coulomb exchange energy.

### 4.3 MODELLING PEAK SHAPES

To precisely quantify positions and linewidths of the spectral features, they have to be modelled using appropriate fitting functions. In PL all peaks, excluding inhomogeneous broadening, follow a lorentzian line shape (see Figure 4.3 A).

$$i(\nu) = \frac{a}{1 + \epsilon^2} \quad (4.2)$$

$$\epsilon = \frac{\nu_0 - \nu}{\gamma/2} \quad (4.3)$$

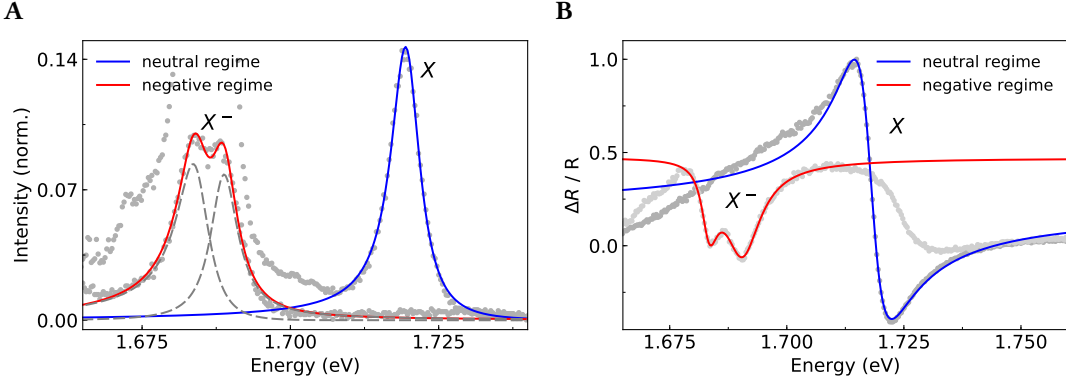


Figure 4.5: Fits of the exciton (X) and trion ( $X^-$ ) features in a neutral and negatively charged spectrum of monolayer  $\text{WSe}_2$ . **A PL**: The lineshape in the fitting model is a lorentzian with adaptive linewidth to model the slight asymmetry of the peaks. It is tuned with a sigmoid function, according to a symmetry parameter. The double-peak of the trion feature is a sum of two asymmetric lorentzians. **B Reflection**: The exciton resonance in this hBN encapsulated sample does not show a clean dip and can be approximated by a model function corresponding to the scattering cross section of a fano resonance. The trion double dip can be fitted using a sum of two asymmetric lorentzians. However, in contrast to the PL fit, a constant shifting parameter is added, and the starting values for the scaling parameter are chosen negative.

where  $i$  denotes the intensity and  $\epsilon$  is the reduced energy, composed of the energy  $\nu$ , the peak position  $\nu_0$  the linewidth  $\gamma$  at FWHM. The maximum value  $a$  scales the peak and normalizes it for a value of 1. In the crowded spectrum of an imperfect sample a pure lorentzian is only an approximation, as the different peaks blend together and can exhibit a substructure, that cannot be resolved as individual features. This leads not only to a broadening of the lines, but also skews the line shape, mostly resulting in a “red shoulder”—higher intensity towards the low-energy end of the peak. To accurately model these features and get good estimates for peak positions as well as linewidths, the functional form of the lorentzian has to be expanded. A generic way of modelling an asymmetric line is to use a lorentzian with variable linewidth  $\gamma$ , meaning the static linewidth of in 4.3 is replaced by a smooth sigmoid function, that includes an additional parameter that scales the asymmetry [75].

$$\gamma = \frac{2\gamma_0}{1 + e^{k(\nu - \nu_0)}} \quad (4.4)$$

This value is then inserted into (4.3). The symmetry parameter  $k$  scales the steepness of the s-curve sigmoid function and thus the skewedness of the lineshape. The  $\gamma_0$  parameter is identical to  $\gamma$  at  $\nu_0$  and corresponds to the peaks linewidth, just like before. For  $k = 0$  (4.3) collapses to  $\gamma_0$  and the standard lorentz lineshape is recovered. The asymmetric lorentzian can be used to model all peaks in the PL spectrum.

In reflection spectroscopy, the signal should correspond to the absorption of the sample. Therefore the straight forward way to model the features would be to use a lorentzian func-

tion as well, only with a negative sign<sup>1</sup>. However, in an hBN-encapsulated sample, the spectrum can be more complicated (see Figure 4.4). The neutral exciton resonance has a highly asymmetric lineshape, that cannot be modeled by a bare lorentzian (either (4.3) or (4.4)). A more general function is the lineshape of a fano resonace. The physical background is the interference between a narrow resonance and a continuous background [76]. In case of encapsulated TMDC monolayers, this lineshape stems from the additional hBN layer below the sample, that forms a microcavity with the underlying reflective Si/SiO<sub>2</sub> substrate [74].

$$\frac{(q + \epsilon)^2}{1 + \epsilon^2} = 1 + \frac{q^2 + 2q\epsilon - 1}{1 + \epsilon^2} \quad (4.5)$$

where  $q$  is the so-called fano parameter. This can be seen as a more general form of (4.3). For  $q = 0$  the shape of (4.5) reduces to a downwards facing lorentzian shifted by one. Just like for the trion and all PL features, the linewidth parameter for (4.4) can be deployed to skew the function to better fit real data.

The trion signal in the charged spectrum shows a double dip. While each individual trion sip shows a fano-type lineshape just as for the neutral exciton, the close proximity of both signals and the strong background complicate the correct estimation of the peak position. Therefore a negative asymmetric loretzian is the naive but effective choice. To compensate for the strong background of the neutral resonance, a constant parameter is added, that gives the peaks a positive offset. Examples of the fitting process for reflection and PL spectra can be seen in figure 4.5. To use the explained fitting functions, the data was sliced to isolate and fit each feature. This makes the minimum and maximum in the energy scale additional parameters that in practice strongly influence the convergence behaviour of the fitting algorithm. However, the disentanglement of the individual peaks makes it easier to finetune the models parameters, so that the most accurate estimate can be found.

#### 4.4 MEASURING THE VALLEY ZEEMAN EFFECT

As described in section 2.4 the band gap and exciton energies in TMDCs shift when exposed to an out-of-plane magnetic field. These shifts are reversed in light of opposite helicity and differ for different types of excitonic processes. Measuring the splitting, and quantifying it through the  $g$ -factor can yield a deeper insight in the nature of the spectral features. Figure 4.10 and 4.11 show the PL and reflection spectra for different gate voltages at 0 and 8 T. Because of different magnetic shifts of the different peaks, looking at  $\sigma^+$  and  $\sigma^-$  polarized spectra at high magnetic field can help to resolve features, that are otherwise hidden by inhomogeneous broadening. The first interesting feature to study in this fashion is the two trion peaks ( $X^-$ ). At 8 T they reveal significant change in their splitting, merging to one peak in  $\sigma^+$  while showing a clear splitting in  $\sigma^-$ . As will be discussed later on, this difference is so far unaccounted for but may be coupled to the asymmetry in intensity when the gate-voltage is swept.

The trion fine structure is a result of electron-electron exchange interaction. The singlet-state consists of an exciton and an electron of opposite spin at the  $K$ -point while the triplet

---

<sup>1</sup>The sign of the fitting functions depends on the definition of the spectrum itself. In this work, the background is subtracted from the signal, yielding the reflection off the flake. A flipped sign on the other hand corresponds to the absorption.

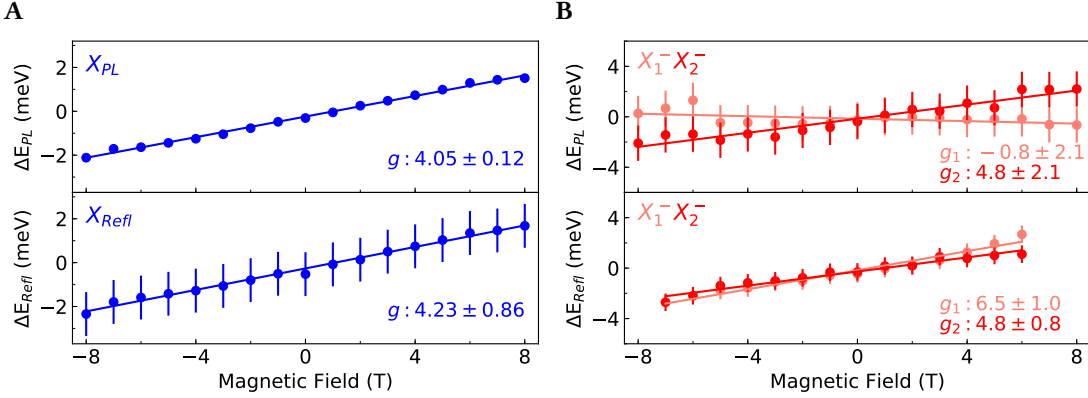


Figure 4.6: Exciton valley Zeeman shift of monolayer WSe<sub>2</sub> in PL and reflection. **A** The *g*-factor of the neutral exciton is in good agreement with previous studies and theoretical prediction. **B** The trion double-feature has a lower error in the reflection spectrum because of a better signal-to-noise. Both measurements suggest different *g*-factors for the two subfeatures.

state involves an additional electron in the  $K'$ -valley, but with the same spin component as the electron in the exciton. The spin-parallel triplet state has a lower binding energy, which allows to also observe the different behavior with regards to the charge density. At high negative gate voltages, both peaks are less intense with the blue peak losing signal much more rapidly. The reasons for that are speculative at best. Recent measurements in WS<sub>2</sub> point to the singlet state being stable only at low temperatures [77]. Similarly, the triplet state in WSe<sub>2</sub> could be more sensitive to large densities of free charge carriers. How this connects to their difference in magnetic moment is unclear.

The magnetic splitting  $\Delta E$  can be quantified by the *g*-factor. Because  $\Delta E$  is linear in magnetic field strength  $B$ , the peak positions can be fitted using simple linear regression where the slope is connected to the *g*-factor in the following fashion:

$$g = \frac{1}{\mu_B} \underbrace{\frac{\Delta E}{\Delta B}}_{slope} \quad (4.6)$$

$$\Delta E = E_{\sigma^+} - E_{\sigma^-} \quad (4.7)$$

Because the splitting is a lot smaller than the linewidth—0.25 meV / T at a linewidth of 7 meV—the peaks have to be fitted using the procedures described in 4.3 to obtain a low error and therefore an accurate estimate for the *g*-factor. Not all features can be resolved well enough, because of either a bad signal to noise ratio or linewidth-related blending with other peaks.

The *g*-factor of the neutral exiton and trion resonances can be measured in both PL and reflection spectroscopy (see figure 4.6). This helps to cross-check experimental results. In case of the neutral exciton, both methods yield a *g*-factor that aligns well with many previous studies

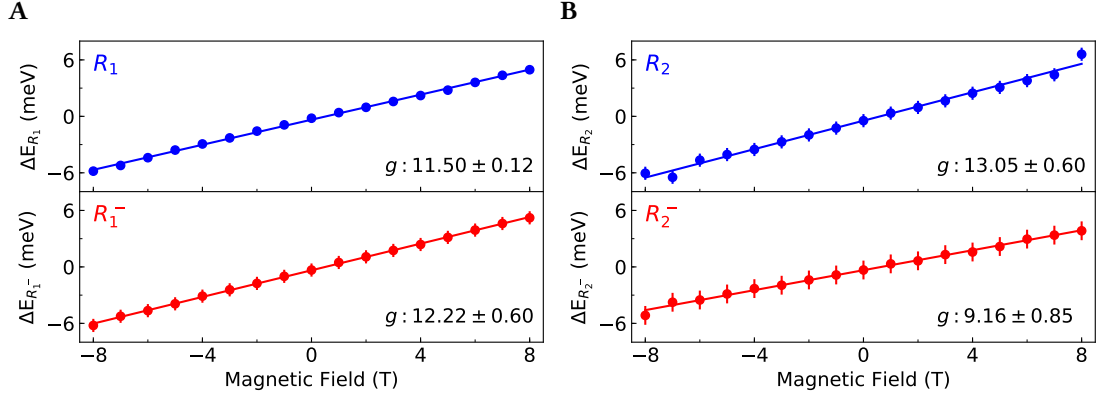


Figure 4.7: Valley Zeeman shift of phonon sidebands in monolayer WSe<sub>2</sub>. **A** The intense  $R_1$  peak and its charged counterpart  $R_1^-$  show a similar  $g$ -factor, suggesting the same origin. This is consistent with the proposed model, that identifies the peaks as acoustic sidebands of momentum-indirect excitons in the  $Q$ -valley.  $R_1$  is of particular interest, because this feature conventionally is attributed to the trion. The strong difference in the  $g$ -factor however suggests a different origin than the trion feature, even though they share the same energy in the spectrum. **B** The neutral peak  $R_2$  was previously identified as a phonon sideband of the  $K'$ -indirect exciton. The high  $g$ -factor however does not offer a direct argument to support this assumption. However, the charged counterpart  $R_2^-$  has a similar  $g$ -factor as was previously measured for  $D$ , which underscores the assumption of the feature being the charged spin-unlike exciton in  $K$ .

[43, 78–80] and also with each other. The fits of the reflection spectra carry a relatively high error. The error bars were estimated by eye using plots to determine deviation of the lineshape from the peaks maxima and minima. Because these errors are much higher than the standard deviation it is fair to say, that they only provide a coarse upper bound. They most likely origin from the substantial deviation of the lineshape from the ideal fano-resonance on the blue and red shoulder.

The trion resonance is much more easy to measure in reflection. The reason for this is partly the bad signal to noise ratio of its PL signal, that can be linked to the longer lifetime of the charged state [81]. But another factor seems to be the limited resolution due to the linewidth of the peaks. The two peaks in the reflection spectrum are separated by roughly 2 meV more, than in PL. The reason for that could simply be the fact, that the lorentzian fit does not really reflect the proper lineshape in the reflection spectrum. Fitting the trion absorption with a double fano lineshape could possibly resolve this difference. For the calculation of the  $g$ -factor this should however not make a difference.

While the trion fits carry a significant error—also in reflection—they clearly show a different  $g$ -factor for each of its features. Since the decay of the trion leaves one free electron behind, it makes sense, that the trion features show the same  $g$ -factor as X. Nonetheless, this difference has also been observed in WS<sub>2</sub> samples at even higher magnetic fields, suggesting a non

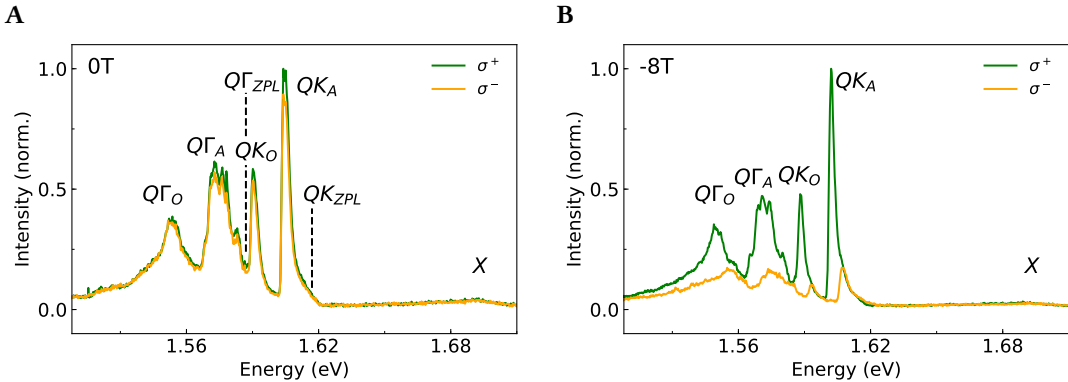


Figure 4.8: PL spectrum of bilayer WSe<sub>2</sub> at 0 and -8 T. **A** Because of the indirect band gap, the PL spectrum is mostly composed of phonon sidebands of momentum-indirect excitons. Because excitons with an electron in Q and a hole in K and  $\Gamma$  have the lowest energy, they should also exhibit the highest population and contribute most to the spectral lines. The zero-phonon line of  $Q\Gamma$  lies around 103 meV below the direct transition X, that is shifted by around 36 meV with respect to the monolayer. The ZPL of  $QK$  is around 30 meV above  $Q\Gamma$ . **B** In a strong magnetic field the valleys split as they do in the monolayer, but the population of the excitation states is "thermal", meaning they distribute according to Boltzman statistics with higher population in the low energy states.

negligible influence of the excess electron towards the total magnetic moment [78].

Having the uncertainty in mind we can compare the trion g-factor to the strong  $R_1$  peak in the neutral spectrum (see figure 4.7). Because it has the same energy as the trion, it is easy to misidentify both features as the same peak and attribute them to the trion. Especially if the sample has no gate control intrinsic electron doping offers a qualitative but not accurate argument for this identification. The magnetic field measurements however show a clear difference between their respective valley splitting. As stated, the g-factor of the trion is hard to determine in PL and has a large error. However, it is bound between 0 and around 6 which is half of the g-factor of  $R_1$ . The strong mismatch can also be observed qualitatively in 4.10.

Unfortunately this leaves the question about the origin of the high g-factor of  $R_1$  open. As briefly discussed in section 2.4 the momentum indirect exciton in Q should not have a g-factor at all, when only looking at the orbital and spin contributions. The effective mass for electrons at the Q-point has however not been calculated for this thesis and therefore the theoretical model predicting the g-factor still has to be completed. This is similar for the  $K'$  indirect exciton and the corresponding peak  $R_2$ , that should be composed of its acoustic phonon sidebands. When counting the orbital and spin contributions it should have the same g-factor as X. That this is not the case means, that a more thorough theoretical understanding is necessary to verify or falsify the identification of the peak.

When looking at the charged spectrum, the g-factor of  $R_1^-$  matches that of  $R_1$  within the  $2\sigma$ -range. Because their distance in energy to X and  $X^-$  also fits, it is reasonable to regard the

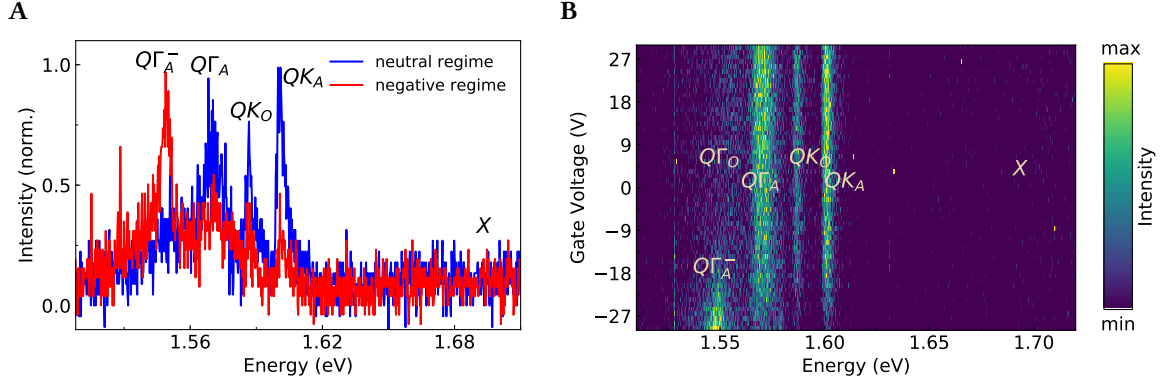


Figure 4.9: Behavior of bilayer WSe<sub>2</sub> at different doping levels. In a negative environment trions form analogous to the monolayer that cause the spectral lines to shift by the trion binding energy. **A** This is most clear for charged peak corresponding to acoustic sidebands of  $Q\Gamma$  with a binding energy of 23 meV. **B** All other peaks also jump by the same energy.

peaks as neutral and charged version of the same momentum-indirect exciton in  $Q$ .

As discussed in the previous section, the second peak  $R_2^-$  energetically matches the spin-unlike but direct dark exciton  $D$ . Therefore it is no wonder, that this is reflected in the significantly smaller  $g$ -factor with respect to the phonon sideband peaks. While it is higher than the value predicted in section 2.4, it is close to what was reported for the neutral dark exciton [34].

#### 4.5 COMPARISON TO BILAYER WSe<sub>2</sub>

As pointed out in section 2.5, bilayer WSe<sub>2</sub> has an indirect band gap and most of the weaker PL can be attributed to the decay of momentum-indirect excitons. The energetically lowest lying excitonic states  $Q\Gamma$  and  $QK$  should have the highest population and that their phonon sidebands therefore should show the highest intensity in the spectrum. The zero-phonon line (ZPL) that corresponds to the energy of the state cannot be seen in the spectrum. Determining their position works analogously to the monolayer by inferring it from the energy of their assumed sidebands. The phonon energies in this case are assumed to be the same as in the monolayer (see 2.3). Following [46] the two blue-most peaks in the spectrum (see figure 4.8) are identified as acoustic and optical sidebands of  $QK$  respectively. The same is done for the two peaks to the red, corresponding to sidebands from  $Q\Gamma$ . Because the  $Q$  valley is around halfway between  $\Gamma$  and  $K$  the necessary quasi-momentum connecting  $QK$  and  $Q\Gamma$  is very close and their phonon sidebands are constructed with energies of phonon modes in  $Q$ . To find the ZPL with respect to the main exciton transition its weak but clear peak can be fitted for reference. In this case  $X$  shifts 36 meV compared to the monolayer part on the same sample. The ZPL of  $QK$  and  $Q\Gamma$  lie around 73 and 103 meV below  $X$  respectively.

While this identification fits the observation of four clear features it is easy to notice, that especially the two red-most peaks have a complex substructure. This is most likely the result

	Monolayer							Bilayer			
	X	R <sub>1</sub>	R <sub>2</sub>	X <sub>1</sub> <sup>-</sup>	X <sub>2</sub> <sup>-</sup>	R <sub>1</sub> <sup>-</sup>	R <sub>2</sub> <sup>-</sup>	QK <sub>A</sub>	QK <sub>O</sub>	QΓ <sub>A</sub>	QΓ <sub>O</sub>
PL	4.05 ± 0.12	11.50 ± 0.12	13.05 ± 0.60	-0.8 ± 2.1	4.8 ± 2.1	12.22 ± 0.60	9.16 ± 0.85	12.12 ± 0.17	10.59 ± 0.24	9.55 ± 0.35	11.90 ± 0.1
Refl.	4.23 ± 0.86	- -	- -	6.5 ± 1.0	4.8 ± 0.8	- -	- -	- -	- -	- -	- -

Table 4.1: Summary of  $g$ -factors for WSe<sub>2</sub> mono- and bilayer, as measured on the same sample with corresponding errors. Since there was only one data-point for the bilayer, errors on the  $g$ -factor are purely derived from the fitting parameters—their true error probably exceeds these values. Having 17 data-points for the monolayer computation means, that a more realistic error could be estimated by watching the variation from point to point.

of higher-order phonon sidebands from QK. Energetically the peaks are closest to what would be combinations of one acoustic and optical phonon more to the blue and processes coupling two optical phonons to the red. However, there is a large number of possible combinations and trying to identify specific higher order phonon sidebands in this spectrum is rather speculative and not unambiguous.

To compare these lines to the possible phonon sidebands of the monolayer this sample was also analyzed at a high negative magnetic field. Since there is no theoretical prediction for the  $g$ -factors of momentum-indirect excitons in the monolayer, the hope of this comparison is, that the  $g$ -factors in the bilayer—that is known to show indirect excitons—can substitute the theoretical prediction. Because taking spectra of bilayer samples demands longer integration times only one data-point was taken, which makes quantifying the uncertainty of the  $g$ -factor less accurate. The peaks can be fitted with an asymmetric lorentzian as well, that can account for the high asymmetry due to their blue shoulder. This shape might seem strange at first, but makes sense, when comparing the PL of a WSe<sub>2</sub> bilayer with other indirect band gap semiconductors [18]. In contrast to single photon process that is only possible if the exciton has no net momentum, all momentum-indirect excitons, whose kinetic energy is distributed thermally can decay radiatively and contribute to their spectral line. This becomes even more clear when looking at the intensity of the peaks when applying a magnetic field (see figure 4.8). The exciton population is pumped at the 2s-resonance. As the lines split because of the valley Zeeman effect, these states decay into lower lying momentum-indirect excitons according to Boltzman statistics. As seen in the graph, the intensity of the higher energy peak of each pair does not exceed the intensity of the lower one, whose exponential flank acts as an envelope for both populations. The band gap minus the exciton binding energy marks the lowest possible energy, which cuts off the peak at its maximum. This behavior is very different from the monolayer, where also the phonon sideband peaks have a similar lineshape as single-phonon peaks like the neutral exciton and trion. Also their intensity ratio does not change as significantly when the lines split in magnetic field and see a raised intensity in the high energy peaks. This

#### *4 Spectroscopy of a WSe<sub>2</sub> gate device*

behavior has been observed before and its origin remains an open question [9]. All  $g$ -factors are listed in table 4.1. As discussed in the previous section, the peak  $R_1$  in the monolayer spectrum is associated with acoustic sidebands of momentum-indirect excitons in the  $Q$ -valley. This corresponds to the blue-most feature in the spectrum of the bilayer ( $QK_A$ ). Their  $g$ -factor is off by about 0.5, which is close enough to suspect a relation of the two spectral lines.

The tuning to the negative regime is another useful comparison between mono- and bilayer WSe<sub>2</sub> (see figure 4.9). At a high negative voltage the behavior is quite similar in that at a certain point the spectral lines loose intensity and reappear redshifted by the trion binding energy. The sample used for this measurement unfortunately was destroyed after the voltage was set to high. Nevertheless this “jump” can be seen clearly for the  $Q\Gamma_A$  peak—corresponding to acoustic sidebands of  $Q\Gamma$ —whose trion counterpart appears red to  $Q\Gamma_O$ . Despite the bad signal-to-noise ratio there are also signature of an onset of the trion counterpart of the peaks to the blue. However, a fresh sample with better gate-tunability might reveal the transition to a charged regime more clearly.

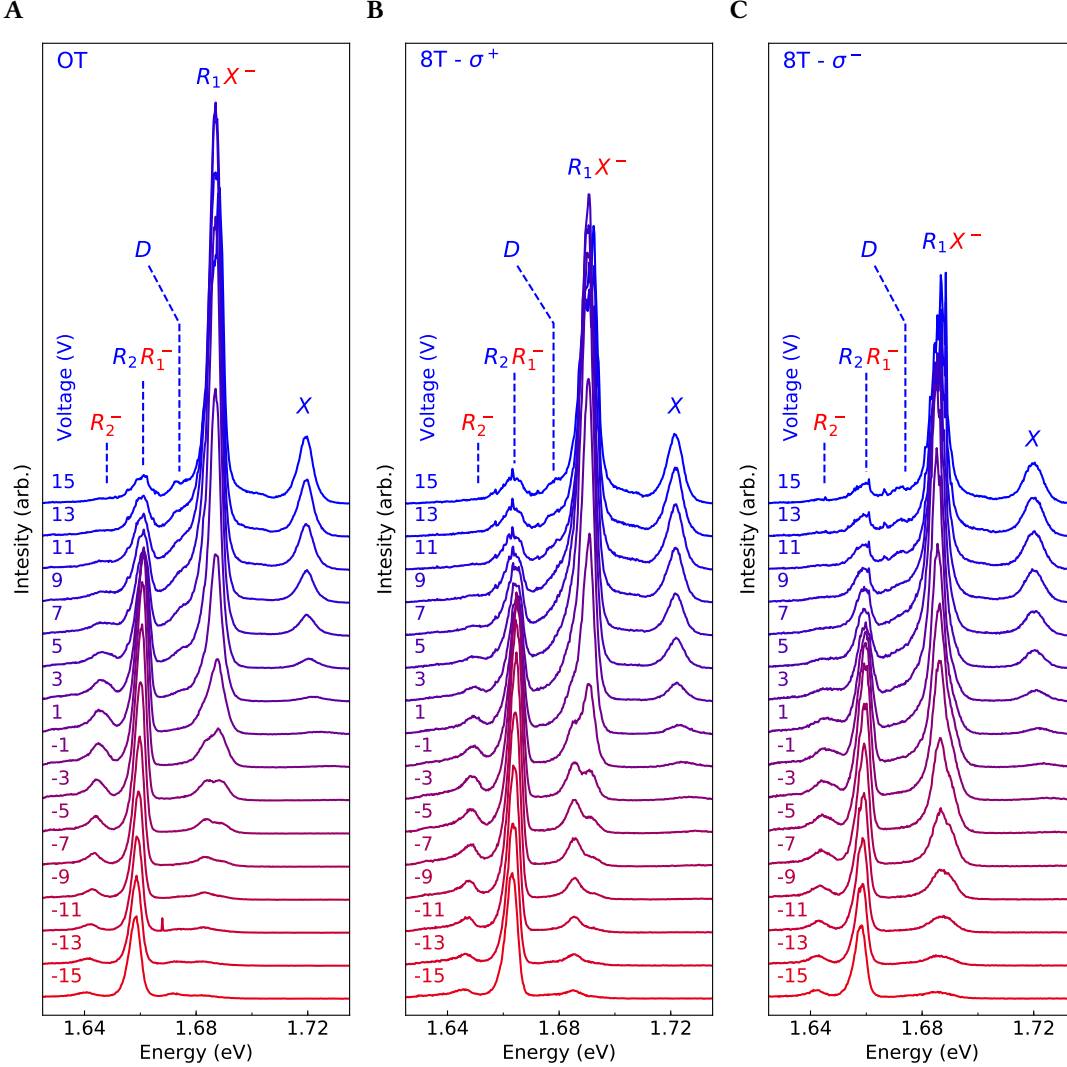


Figure 4.10: PL spectra of WSe<sub>2</sub> at high magnetic fields for different gate voltages. The transition between the strong phonon sideband  $R_1$  to the trion  $X^-$  can be observed. Apart from the exchange splitting of the trion, their different nature can be also seen by looking at the spectrum at 8 T. The splitting of  $R_1$  is much stronger than that of  $X^-$ , such that in the transition around 1–5 V the trion appears as a red shoulder in  $\sigma^+$  and a blue shoulder in  $\sigma^-$ . The two features of  $X^-$  by themselves also behave very differently. Not only do they appear to have a different g-factor, but they also are very asymmetric with regards to their intensity and how it is lowered for high negative doping.

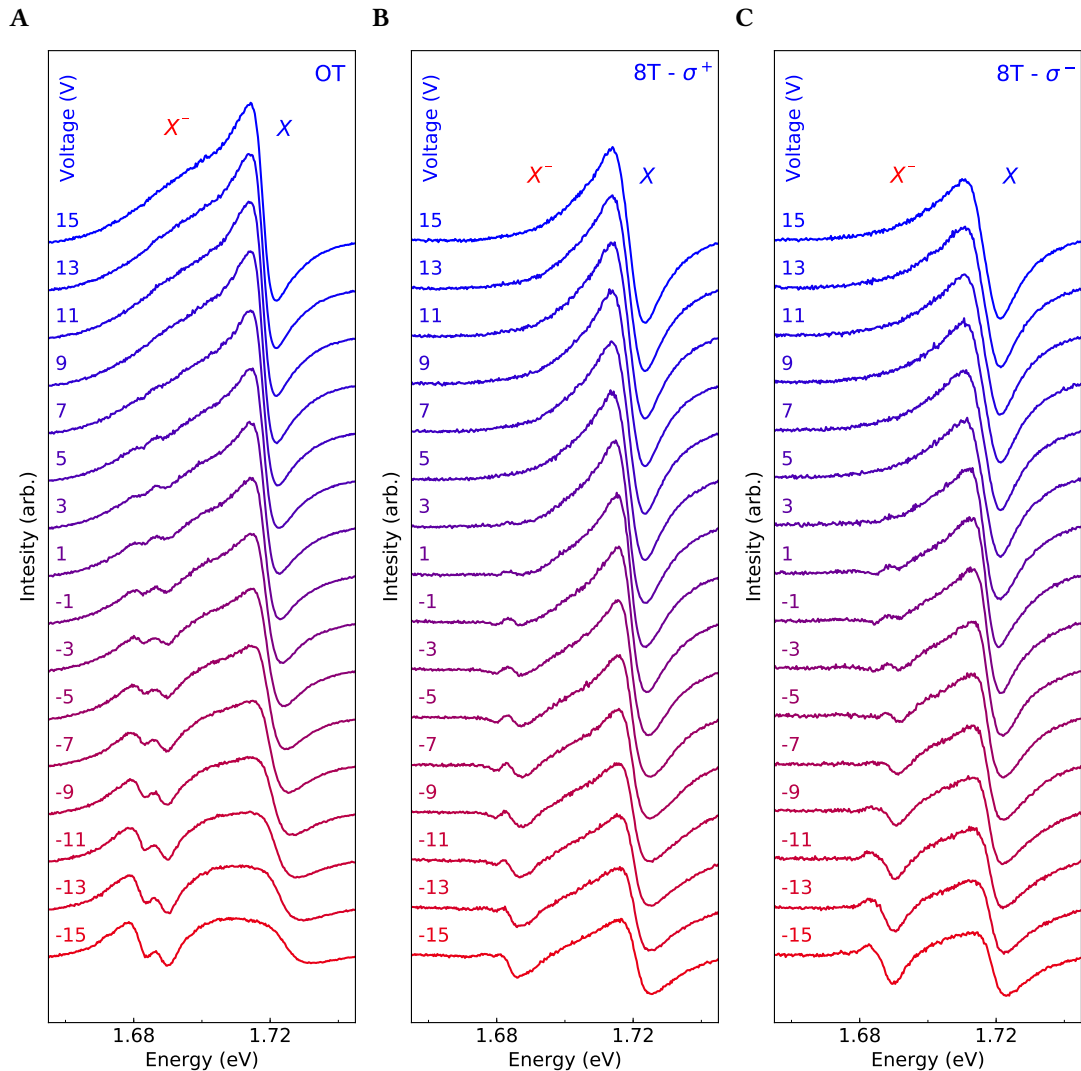


Figure 4.11: Reflection spectra for different gate voltages at high magnetic fields. The comparison between  $\sigma^+$  and  $\sigma^-$  shows the asymmetry of the trion resonance, whose two features shift by a different amount resulting in two different line shapes at 8 T. This reason for this difference in the  $g$ -factor has yet to be determined.

## 5 SUMMARY & OUTLOOK

The goal of this thesis was to establish a fabrication process to produce TMDC monolayers of high optical quality by means of encapsulation in hBN and active control of the charge doping level. This was accomplished by combining the dry transfer technique of “hot pick-up and stamping” [52, 62] with contact lithography and mechanical exfoliation. TMD monolayers were produced by mechanically exfoliating material from a bulk crystal with adhesive tape. To obtain narrow linewidths they were encapsulated in hBN flakes by picking up hBN and TMDC flakes one by one with a PPC-coated PDMS-stamp and dropped in contact with gold electrodes. To verify the function and determine the maximum gate voltage the leaking current through the samples was measured using a lock-in technique.

A combined gate-tunable mono- and bilayer sample of tungsten diselenide was analyzed by means of confocal spectroscopy. Both reflection and photoluminescence spectra were recorded while sweeping the gate voltage to determine intrinsic doping and observe the transition between neutral and negative charge carrier density [82].

The observed spectral linewidth of 6–7 meV for the neutral exciton peak is a significant improvement over previous samples, especially because these values can be observed on most of the sample. The intrinsic homogeneous linewidth is expected to be below 2 meV [73], so there is still room for improvement.

The good linewidth-related resolution allowed the study of different spectral features while tuning the electron density as well as applying a magnetic field. As a result the transition between a neutral regime and a negatively charged regime could be observed [82], in which the neutral exciton peak vanishes along with peaks to the red, that are associated with momentum-indirect excitons. Instead, the trion double feature, that is split by exchange interaction appears 30 meV to the red of the exciton, along with a new set of phonon sidebands, that could be charged counterparts of the peaks in the neutral spectrum. The first phonon sideband, associated with a momentum-indirect exciton with an electron in the Q-valley, is energetically close to the trion. Therefore its behavior upon changing the gate voltage was of particular interest. The exchange splitting of 5.2 meV upon the transition to the charged regime as well as a g-factor of 11.5 show that this peak is different from the trion. The spectral line associated with the same phonon sideband in the bilayer shows a similar g-factor of 12.1, which suggests a relation between both features and is an argument for the phonon sideband model.

The same measurements will also be performed on a sample of tungsten disulfide in the near future.

Other than that, there are also possible advancements in the fabrication process and sample engineering. Uncontrolled thickness of the bottom hBN flake as well as the 50–90 nm SiO<sub>2</sub> dielectric mean, that in order to create significant electric field strengths, high voltages close to breakdown have to be applied to observe the transition between all relevant regimes. It could be instructive to further extend the gate tunability and there are some viable options to over-

## *5 Summary & outlook*

come previous limitations. One option is to integrate top and backgate into the heterostructure itself. Using graphene beneath the bottom hBN flake or above the top, the distance between the gates could be significantly reduced. The result would be a higher field strength close to the sample. The other option would be to retain the substrate as backgate but to discard SiO<sub>2</sub> as as the top layer of the substrate. Using techniques such as atomic layer deposition of materials like aluminum oxide, a thin dielectric can be fabricated [83]. A thinner dielectric layer would increase the possible field strength with less complexity of the van-der-Waals heterostructure.

Additionally there are new types of samples that could be fabricated and analyzed. Stacking different TMDC monolayers on top of each other to form gate-tunable heterobilayers could yield a better understanding of features like second-harmonic generation and layer-indirect excitons. A challenge would be to align the crystal axis of the precursor monolayers, but this could also be an opportunity to study moiré effects in more detail, that originate from a lattice mismatch between the two layers. Finally, heterostructures as well as single layer samples could be embedded in an optical micro-cavity while also being fully gate tunable. This could help the understanding of exciton-polaritons and phenomena related to cavity physics of TMDCs

.

## BIBLIOGRAPHY

- <sup>1</sup>K. S. Novoselov, “Electric field effect in atomically thin carbon films”, *Science* **306**, 666–669 (2004).
- <sup>2</sup>Q. H. Wang, K. Kalantar-Zadeh, A. Kis, J. N. Coleman, and M. S. Strano, “Electronics and optoelectronics of two-dimensional transition metal dichalcogenides”, *Nature Nanotechnology* **7**, 699–712 (2012).
- <sup>3</sup>K. F. Mak, K. L. McGill, J. Park, and P. L. McEuen, “The valley hall effect in MoS<sub>2</sub> transistors”, *Science* **344**, 1489–1492 (2014).
- <sup>4</sup>F. Langer, C. P. Schmid, S. Schlauderer, M. Gmitra, J. Fabian, P. Nagler, C. Schüller, T. Korn, P. G. Hawkins, J. T. Steiner, U. Hettner, S. W. Koch, M. Kira, and R. Huber, “Lightwave valleytronics in a monolayer of tungsten diselenide”, *Nature* **557**, 76–80 (2018).
- <sup>5</sup>A. Chernikov, T. C. Berkelbach, H. M. Hill, A. Rigosi, Y. Li, O. B. Aslan, D. R. Reichman, M. S. Hybertsen, and T. F. Heinz, “Exciton binding energy and nonhydrogenic rydberg series in monolayer WS<sub>2</sub>”, *Physical Review Letters* **113** (2014) 10.1103/PhysRevLett.113.076802.
- <sup>6</sup>A. Srivastava, M. Sidler, A. V. Allain, D. S. Lembke, A. Kis, and A. Imamoğlu, “Optically active quantum dots in monolayer WSe<sub>2</sub>”, *Nature Nanotechnology* **10**, 491–496 (2015).
- <sup>7</sup>X. Liu, W. Bao, Q. Li, C. Ropp, Y. Wang, and X. Zhang, “Control of coherently coupled exciton polaritons in monolayer tungsten disulphide”, *Physical Review Letters* **119** (2017) 10.1103/PhysRevLett.119.027403.
- <sup>8</sup>L. Zhang, R. Gogna, W. Burg, E. Tutuc, and H. Deng, “Photonic-crystal exciton-polaritons in monolayer semiconductors”, *Nature Communications* **9** (2018) 10.1038/s41467-018-03188-x.
- <sup>9</sup>M. Koperski, M. R. Molas, A. Arora, K. Nogajewski, A. O. Slobodeniuk, C. Faugeras, and M. Potemski, “Optical properties of atomically thin transition metal dichalcogenides: observations and puzzles”, *Nanophotonics* **6** (2017) 10.1515/nanoph-2016-0165.
- <sup>10</sup>C. R. Dean, A. F. Young, I. Meric, C. Lee, L. Wang, S. Sorgenfrei, K. Watanabe, T. Taniguchi, P. Kim, K. L. Shepard, and J. Hone, “Boron nitride substrates for high-quality graphene electronics”, *Nature Nanotechnology* **5**, 722–726 (2010).
- <sup>11</sup>F. Cadiz, E. Courtade, C. Robert, G. Wang, Y. Shen, H. Cai, T. Taniguchi, K. Watanabe, H. Carrere, D. Lagarde, M. Manca, T. Amand, P. Renucci, S. Tongay, X. Marie, and B. Urbaszek, “Excitonic linewidth approaching the homogeneous limit in MoS<sub>2</sub>-based van der waals heterostructures”, *Physical Review X* **7** (2017) 10.1103/PhysRevX.7.021026.

## BIBLIOGRAPHY

- <sup>12</sup>E. Courtade, M. Semina, M. Manca, M. M. Glazov, C. Robert, F. Cadiz, G. Wang, T. Taniguchi, K. Watanabe, M. Pierre, W. Escoffier, E. L. Ivchenko, P. Renucci, X. Marie, T. Amand, and B. Urbaszek, “Charged excitons in monolayer WSe<sub>2</sub>: experiment and theory”, Physical Review B **96** (2017) 10.1103/PhysRevB.96.085302.
- <sup>13</sup>D. Xiao, G.-B. Liu, W. Feng, X. Xu, and W. Yao, “Coupled spin and valley physics in monolayers of MoS<sub>2</sub> and other group-VI dichalcogenides”, Physical Review Letters **108** (2012) 10.1103/PhysRevLett.108.196802.
- <sup>14</sup>B. Ouyang, G. Lan, Y. Guo, Z. Mi, and J. Song, “Phase engineering of monolayer transition-metal dichalcogenide through coupled electron doping and lattice deformation”, Applied Physics Letters **107**, 191903 (2015).
- <sup>15</sup>E. Cappelluti, R. Roldán, J. A. Silva-Guillén, P. Ordejón, and F. Guinea, “Tight-binding model and direct-gap/indirect-gap transition in single-layer and multilayer MoS<sub>2</sub>”, Physical Review B **88** (2013) 10.1103/PhysRevB.88.075409.
- <sup>16</sup>J. Silva-Guillén, P. San-Jose, and R. Roldán, “Electronic band structure of transition metal dichalcogenides from ab initio and slater-koster tight-binding model”, Applied Sciences **6**, 284 (2016).
- <sup>17</sup>Z. Y. Zhu, Y. C. Cheng, and U. Schwingenschlögl, “Giant spin-orbit-induced spin splitting in two-dimensional transition-metal dichalcogenide semiconductors”, Physical Review B **84** (2011) 10.1103/PhysRevB.84.153402.
- <sup>18</sup>I. Pelant and J. Valenta, *Luminescence spectroscopy of semiconductors* (Oxford University Press, Feb. 9, 2012) Chap. 10.
- <sup>19</sup>A. Hanbicki, M. Currie, G. Kioseoglou, A. Friedman, and B. Jonker, “Measurement of high exciton binding energy in the monolayer transition-metal dichalcogenides WS<sub>2</sub> and WSe<sub>2</sub>”, Solid State Communications **203**, 16–20 (2015).
- <sup>20</sup>K. He, N. Kumar, L. Zhao, Z. Wang, K. F. Mak, H. Zhao, and J. Shan, “Tightly bound excitons in monolayer WSe<sub>2</sub>”, Physical Review Letters **113** (2014) 10.1103/PhysRevLett.113.026803.
- <sup>21</sup>M. Palummo, M. Bernardi, and J. C. Grossman, “Exciton radiative lifetimes in two-dimensional transition metal dichalcogenides”, Nano Letters **15**, 2794–2800 (2015).
- <sup>22</sup>A. V. Stier, N. P. Wilson, G. Clark, X. Xu, and S. A. Crooker, “Probing the influence of dielectric environment on excitons in monolayer WSe<sub>2</sub>: insight from high magnetic fields”, Nano Letters **16**, 7054–7060 (2016).
- <sup>23</sup>S. Borghardt, J.-S. Tu, F. Winkler, J. Schubert, W. Zander, K. Leosson, and B. E. Kardynał, “Engineering of optical and electronic band gaps in transition metal dichalcogenide monolayers through external dielectric screening”, Physical Review Materials **1** (2017) 10.1103/PhysRevMaterials.1.054001.
- <sup>24</sup>T. Jakubczyk, K. Nogajewski, M. R. Molas, M. Bartos, W. Langbein, M. Potemski, and J. Kasprzak, “Impact of environment on dynamics of exciton complexes in a WS<sub>2</sub> monolayer”, 2D Materials **5**, 031007 (2018).

- <sup>25</sup>B. Peng, Q. Li, X. Liang, P. Song, J. Li, K. He, D. Fu, Y. Li, C. Shen, H. Wang, C. Wang, T. Liu, L. Zhang, H. Lu, X. Wang, J. Zhao, J. Xie, M. Wu, L. Bi, L. Deng, and K. P. Loh, “Valley polarization of trions and magnetoresistance in heterostructures of MoS<sub>2</sub> and yttrium iron garnet”, ACS Nano **11**, 12257–12265 (2017).
- <sup>26</sup>C. Zhao, T. Norden, P. Zhang, P. Zhao, Y. Cheng, F. Sun, J. P. Parry, P. Taheri, J. Wang, Y. Yang, T. Scrace, K. Kang, S. Yang, G.-x. Miao, R. Sabirianov, G. Kioseoglou, W. Huang, A. Petrou, and H. Zeng, “Enhanced valley splitting in monolayer WSe<sub>2</sub> due to magnetic exchange field”, Nature Nanotechnology **12**, 757–762 (2017).
- <sup>27</sup>T. Smoleński, M. Goryca, M. Koperski, C. Faugeras, T. Kazimierczuk, A. Bogucki, K. Nogajewski, P. Kossacki, and M. Potemski, “Tuning valley polarization in a WSe<sub>2</sub> monolayer with a tiny magnetic field”, Physical Review X **6** (2016) 10.1103/PhysRevX.6.021024.
- <sup>28</sup>A. Neumann, J. Lindlau, L. Colombier, M. Nutz, S. Najmaei, J. Lou, A. D. Mohite, H. Yamaguchi, and A. Högele, “Opto-valleytronic imaging of atomically thin semiconductors”, Nature Nanotechnology **12**, 329–334 (2017).
- <sup>29</sup>N. Zibouche, A. Kuc, J. Musfeldt, and T. Heine, “Transition-metal dichalcogenides for spintronic applications: spintronics beyond graphene”, Annalen der Physik **526**, 395–401 (2014).
- <sup>30</sup>J. Lindlau, C. Robert, V. Funk, J. Förste, M. Förög, L. Colombier, A. Neumann, E. Courtade, S. Shree, T. Taniguchi, K. Watanabe, M. M. Glazov, X. Marie, B. Urbaszek, and A. Högele, “Identifying optical signatures of momentum-dark excitons in transition metal dichalcogenide monolayers”, arXiv:1710.00988 [cond-mat] (2017).
- <sup>31</sup>Z. Jin, X. Li, J. T. Mullen, and K. W. Kim, “Intrinsic transport properties of electrons and holes in monolayer transition-metal dichalcogenides”, Physical Review B **90** (2014) 10.1103/PhysRevB.90.045422.
- <sup>32</sup>C. R. Zhu, G. Wang, B. L. Liu, X. Marie, X. F. Qiao, X. Zhang, X. X. Wu, H. Fan, P. H. Tan, T. Amand, and B. Urbaszek, “Strain tuning of optical emission energy and polarization in monolayer and bilayer MoS<sub>2</sub>”, Physical Review B **88** (2013) 10.1103/PhysRevB.88.121301.
- <sup>33</sup>J. P. Echeverry, B. Urbaszek, T. Amand, X. Marie, and I. C. Gerber, “Splitting between bright and dark excitons in transition metal dichalcogenide monolayers”, Physical Review B **93** (2016) 10.1103/PhysRevB.93.121107.
- <sup>34</sup>C. Robert, T. Amand, F. Cadiz, D. Lagarde, E. Courtade, M. Manca, T. Taniguchi, K. Watanabe, B. Urbaszek, and X. Marie, “Fine structure and lifetime of dark excitons in transition metal dichalcogenide monolayers”, Physical Review B **96** (2017) 10.1103/PhysRevB.96.155423.
- <sup>35</sup>G. Wang, C. Robert, M. M. Glazov, F. Cadiz, E. Courtade, T. Amand, D. Lagarde, T. Taniguchi, K. Watanabe, B. Urbaszek, and X. Marie, “In-plane propagation of light in transition metal dichalcogenide monolayers: optical selection rules”, Physical Review Letters **119** (2017) 10.1103/PhysRevLett.119.047401.
- <sup>36</sup>M. Sidler, P. Back, O. Cotlet, A. Srivastava, T. Fink, M. Kroner, E. Demler, and A. Imamoglu, “Fermi polaron-polaritons in charge-tunable atomically thin semiconductors”, Nature Physics **13**, 255–261 (2016).

## BIBLIOGRAPHY

- <sup>37</sup>D. K. Efimkin and A. H. MacDonald, “Many-body theory of trion absorption features in two-dimensional semiconductors”, *Physical Review B* **95** (2017) 10 . 1103/PhysRevB.95.035417.
- <sup>38</sup>R. Schmidt, T. Enss, V. Pietilä, and E. Demler, “Fermi polarons in two dimensions”, *Physical Review A* **85** (2012) 10 . 1103/PhysRevA.85.021602.
- <sup>39</sup>T. Kato and T. Kaneko, “Optical detection of a highly localized impurity state in monolayer tungsten disulfide”, *ACS Nano* **8**, 12777–12785 (2014).
- <sup>40</sup>S. Zhang, C.-G. Wang, M.-Y. Li, D. Huang, L.-J. Li, W. Ji, and S. Wu, “Defect structure of localized excitons in a WSe<sub>2</sub> monolayer”, *Physical Review Letters* **119** (2017) 10 . 1103 / PhysRevLett.119.046101.
- <sup>41</sup>C. Zhang, Y. Chen, A. Johnson, M.-Y. Li, L.-J. Li, P. C. Mende, R. M. Feenstra, and C.-K. Shih, “Probing critical point energies of transition metal dichalcogenides: surprising indirect gap of single layer WSe<sub>2</sub>”, *Nano Letters* **15**, 6494–6500 (2015).
- <sup>42</sup>W.-T. Hsu, L.-S. Lu, D. Wang, J.-K. Huang, M.-Y. Li, T.-R. Chang, Y.-C. Chou, Z.-Y. Juang, H.-T. Jeng, L.-J. Li, and W.-H. Chang, “Evidence of indirect gap in monolayer WSe<sub>2</sub>”, *Nature Communications* **8** (2017) 10 . 1038/s41467-017-01012-6.
- <sup>43</sup>A. Srivastava, M. Sidler, A. V. Allain, D. S. Lembke, A. Kis, and A. Imamoğlu, “Valley zeeman effect in elementary optical excitations of monolayer WSe<sub>2</sub>”, *Nature Physics* **11**, 141–147 (2015).
- <sup>44</sup>G. Aivazian, Z. Gong, A. M. Jones, R.-L. Chu, J. Yan, D. G. Mandrus, C. Zhang, D. Cobden, W. Yao, and X. Xu, “Magnetic control of valley pseudospin in monolayer WSe<sub>2</sub>”, *Nature Physics* **11**, 148–152 (2015).
- <sup>45</sup>D. V. Rybkovskiy, I. C. Gerber, and M. V. Durnev, “Atomically inspired  $k \cdot p$  approach and valley zeeman effect in transition metal dichalcogenide monolayers”, *Physical Review B* **95** (2017) 10 . 1103/PhysRevB.95.155406.
- <sup>46</sup>J. Lindlau, M. Selig, A. Neumann, L. Colombier, J. Kim, G. Berghäuser, F. Wang, E. Malic, and A. Högele, “The role of momentum-dark excitons in the elementary optical response of bilayer WSe<sub>2</sub>”, arXiv:1710.00989 [cond-mat] (2017).
- <sup>47</sup>A. M. Jones, H. Yu, J. S. Ross, P. Klement, N. J. Ghimire, J. Yan, D. G. Mandrus, W. Yao, and X. Xu, “Spin-layer locking effects in optical orientation of exciton spin in bilayer WSe<sub>2</sub>”, *Nature Physics* **10**, 130–134 (2014).
- <sup>48</sup>N. R. Wilson, P. V. Nguyen, K. Seyler, P. Rivera, A. J. Marsden, Z. P. Laker, G. C. Constantinescu, V. Kandyba, A. Barinov, N. D. Hine, X. Xu, and D. H. Cobden, “Determination of band offsets, hybridization, and exciton binding in 2d semiconductor heterostructures”, *Science Advances* **3**, e1601832 (2017).
- <sup>49</sup>V. Funk, “Spectroscopy of momentum-dark excitons in layered semiconductors” (LMU München, 2017).
- <sup>50</sup>J. Chen, W. Tang, B. Tian, B. Liu, X. Zhao, Y. Liu, T. Ren, W. Liu, D. Geng, H. Y. Jeong, H. S. Shin, W. Zhou, and K. P. Loh, “Chemical vapor deposition of high-quality large-sized MoS<sub>2</sub> crystals on silicon dioxide substrates”, *Advanced Science* **3**, 1500033 (2016).

- <sup>51</sup>A. K. Geim and K. S. Novoselov, “The rise of graphene”, *Nature Materials* **6**, 183–191 (2007).
- <sup>52</sup>F. Pizzocchero, L. Gammelgaard, B. S. Jessen, J. M. Caridad, L. Wang, J. Hone, P. Bøggild, and T. J. Booth, “The hot pick-up technique for batch assembly of van der waals heterostructures”, *Nature Communications* **7**, 11894 (2016).
- <sup>53</sup>W. Zhao, Z. Ghorannevis, K. K. Amara, J. R. Pang, M. Toh, X. Zhang, C. Kloc, P. H. Tan, and G. Eda, “Lattice dynamics in mono- and few-layer sheets of WS<sub>2</sub> and WSe<sub>2</sub>”, *Nanoscale* **5**, 9677 (2013).
- <sup>54</sup>X. Zhang, X.-F. Qiao, W. Shi, J.-B. Wu, D.-S. Jiang, and P.-H. Tan, “Phonon and raman scattering of two-dimensional transition metal dichalcogenides from monolayer, multilayer to bulk material”, *Chemical Society Reviews* **44**, 2757–2785 (2015).
- <sup>55</sup>P. Tonndorf, R. Schmidt, P. Böttger, X. Zhang, J. Börner, A. Liebig, M. Albrecht, C. Kloc, O. Gordan, D. R. T. Zahn, S. Michaelis de Vasconcellos, and R. Bratschitsch, “Photoluminescence emission and raman response of monolayer MoS<sub>2</sub>, MoSe<sub>2</sub>, and WSe<sub>2</sub>”, *Optics Express* **21**, 4908 (2013).
- <sup>56</sup>E. Courtade, B. Han, S. Nakhaie, C. Robert, X. Marie, P. Renucci, T. Taniguchi, K. Watanabe, L. Geelhaar, J. M. J. Lopes, and B. Urbaszek, “Spectrally narrow exciton luminescence from monolayer MoS<sub>2</sub> exfoliated onto epitaxially grown hexagonal BN”, arXiv:1804.06623 [cond-mat] (2018).
- <sup>57</sup>B. Arnaud, S. Lebègue, P. Rabiller, and M. Alouani, “Huge excitonic effects in layered hexagonal boron nitride”, *Physical Review Letters* **96** (2006) 10.1103/PhysRevLett.96.026402.
- <sup>58</sup>J. I.-J. Wang, Y. Yang, Y.-A. Chen, K. Watanabe, T. Taniguchi, H. O. H. Churchill, and P. Jarillo-Herrero, “Electronic transport of encapsulated graphene and WSe<sub>2</sub> devices fabricated by pick-up of prepatterned hBN”, *Nano Letters* **15**, 1898–1903 (2015).
- <sup>59</sup>B. Fallahazad, H. C. P. Movva, K. Kim, S. Larentis, T. Taniguchi, K. Watanabe, S. K. Banerjee, and E. Tutuc, “Shubnikov-de haas oscillations of high-mobility holes in monolayer and bi-layer WSe<sub>2</sub>: landau level degeneracy, effective mass, and negative compressibility”, *Physical Review Letters* **116** (2016) 10.1103/PhysRevLett.116.086601.
- <sup>60</sup>H. Li, J. Wu, X. Huang, Z. Yin, J. Liu, and H. Zhang, “A universal, rapid method for clean transfer of nanostructures onto various substrates”, *ACS Nano* **8**, 6563–6570 (2014).
- <sup>61</sup>A. Castellanos-Gomez, M. Buscema, R. Molenaar, V. Singh, L. Janssen, H. S. J. v. d. Zant, and G. A. Steele, “Deterministic transfer of two-dimensional materials by all-dry viscoelastic stamping”, *2D Materials* **1**, 011002 (2014).
- <sup>62</sup>D. H. Tien, J.-Y. Park, K. B. Kim, N. Lee, T. Choi, P. Kim, T. Taniguchi, K. Watanabe, and Y. Seo, “Study of graphene-based 2d-heterostructure device fabricated by all-dry transfer process”, *ACS Applied Materials & Interfaces* **8**, 3072–3078 (2016).
- <sup>63</sup>K.-H. Jung, D. G. Kim, and S.-B. Jung, “Adhesion of PDMS substrates assisted by plasma graft polymerization”, *Surface and Interface Analysis* **48**, 597–600 (2016).
- <sup>64</sup>Y.-C. Lin, C.-C. Lu, C.-H. Yeh, C. Jin, K. Suenaga, and P.-W. Chiu, “Graphene annealing: how clean can it be?”, *Nano Letters* **12**, 414–419 (2012).

## BIBLIOGRAPHY

- <sup>65</sup>N. Klein and H. Gafni, "The maximum dielectric strength of thin silicon oxide films", IEEE Transactions on Electron Devices **ED-13**, 281–289 (1966).
- <sup>66</sup>X. H. Wang, J. Q. Ning, Z. C. Su, C. C. Zheng, B. R. Zhu, L. Xie, H. S. Wu, and S. J. Xu, "Photoinduced doping and photoluminescence signature in an exfoliated WS<sub>2</sub> monolayer semiconductor", RSC Advances **6**, 27677–27681 (2016).
- <sup>67</sup>P. D. Cunningham, A. T. Hanbicki, K. M. McCreary, and B. T. Jonker, "Photoinduced bandgap renormalization and exciton binding energy reduction in WS<sub>2</sub>", ACS Nano **11**, 12601–12608 (2017).
- <sup>68</sup>Y. Kang and S. Han, "An origin of unintentional doping in transition metal dichalcogenides: the role of hydrogen impurities", Nanoscale **9**, 4265–4271 (2017).
- <sup>69</sup>K. Eshun, H. D. Xiong, S. Yu, and Q. Li, "Doping induces large variation in the electrical properties of MoS<sub>2</sub> monolayers", Solid-State Electronics **106**, 44–49 (2015).
- <sup>70</sup>P. K. Chow, R. B. Jacobs-Gedrim, J. Gao, T.-M. Lu, B. Yu, H. Terrones, and N. Koratkar, "Defect-induced photoluminescence in monolayer semiconducting transition metal dichalcogenides", ACS Nano **9**, 1520–1527 (2015).
- <sup>71</sup>Z. Lin, B. R. Carvalho, E. Kahn, R. Lv, R. Rao, H. Terrones, M. A. Pimenta, and M. Terrones, "Defect engineering of two-dimensional transition metal dichalcogenides", 2D Materials **3**, 022002 (2016).
- <sup>72</sup>G. Moody, C. Kavir Dass, K. Hao, C.-H. Chen, L.-J. Li, A. Singh, K. Tran, G. Clark, X. Xu, G. Berghäuser, E. Malic, A. Knorr, and X. Li, "Intrinsic homogeneous linewidth and broadening mechanisms of excitons in monolayer transition metal dichalcogenides", Nature Communications **6** (2015) 10.1038/ncomms9315.
- <sup>73</sup>O. A. Ajayi, J. V. Ardelean, G. D. Shepard, J. Wang, A. Antony, T. Taniguchi, K. Watanabe, T. F. Heinz, S. Strauf, X.-Y. Zhu, and J. C. Hone, "Approaching the intrinsic photoluminescence linewidth in transition metal dichalcogenide monolayers", 2D Materials **4**, 031011 (2017).
- <sup>74</sup>G. Scuri, Y. Zhou, A. A. High, D. S. Wild, C. Shu, K. De Greve, L. A. Jauregui, T. Taniguchi, K. Watanabe, P. Kim, M. D. Lukin, and H. Park, "Large excitonic reflectivity of monolayer MoSe<sub>2</sub> encapsulated in hexagonal boron nitride", Physical Review Letters **120** (2018) 10.1103/PhysRevLett.120.037402.
- <sup>75</sup>A. L. Stancik and E. B. Brauns, "A simple asymmetric lineshape for fitting infrared absorption spectra", Vibrational Spectroscopy **47**, 66–69 (2008).
- <sup>76</sup>U. Fano, "Effects of configuration interaction on intensities and phase shifts", Physical Review **124**, 1866–1878 (1961).
- <sup>77</sup>D. Vaclavkova, J. Wyzula, K. Nogajewski, M. Bartos, A. O. Slobodeniuk, C. Faugeras, M. Potemski, and M. R. Molas, "Singlet and triplet trions in WS<sub>2</sub> monolayer encapsulated in hexagonal boron nitride", arXiv:1802.05538 [cond-mat] (2018).
- <sup>78</sup>G. Plechinger, P. Nagler, A. Arora, A. Granados del Águila, M. V. Ballottin, T. Frank, P. Steinleitner, M. Gmitra, J. Fabian, P. C. M. Christianen, R. Bratschitsch, C. Schüller, and T. Korn, "Excitonic valley effects in monolayer WS<sub>2</sub> under high magnetic fields", Nano Letters **16**, 7899–7904 (2016).

## BIBLIOGRAPHY

- <sup>79</sup>A. V. Stier, K. M. McCreary, B. T. Jonker, J. Kono, and S. A. Crooker, “Exciton diamagnetic shifts and valley zeeman effects in monolayer WS<sub>2</sub> and MoS<sub>2</sub> to 65 tesla”, *Nature Communications* **7**, 10643 (2016).
- <sup>80</sup>A. A. Mitioglu, K. Galkowski, A. Surrente, L. Klopotowski, D. Dumcenco, A. Kis, D. K. Maude, and P. Plochocka, “Magnetoexcitons in large area CVD-grown monolayer MoS<sub>2</sub> and MoSe<sub>2</sub> on sapphire”, *Physical Review B* **93** (2016) 10.1103/PhysRevB.93.165412.
- <sup>81</sup>K. Hao, L. Xu, F. Wu, P. Nagler, K. Tran, X. Ma, C. Schüller, T. Korn, A. H. MacDonald, G. Moody, and X. Li, “Trion valley coherence in monolayer semiconductors”, *2D Materials* **4**, 025105 (2017).
- <sup>82</sup>Z. Wang, L. Zhao, K. F. Mak, and J. Shan, “Probing the spin-polarized electronic band structure in monolayer transition metal dichalcogenides by optical spectroscopy”, *Nano Letters* **17**, 740–746 (2017).
- <sup>83</sup>S. Jandhyala, G. Mordi, B. Lee, G. Lee, C. Floresca, P.-R. Cha, J. Ahn, R. M. Wallace, Y. J. Chabal, M. J. Kim, L. Colombo, K. Cho, and J. Kim, “Atomic layer deposition of dielectrics on graphene using reversibly physisorbed ozone”, *ACS Nano* **6**, 2722–2730 (2012).



# DANKSAGUNG



# **ERKLÄRUNG**

Hiermit erkläre ich, die vorliegende Arbeit selbständig verfasst zu haben und keine anderen als die in der Arbeit angegebenen Quellen und Hilfsmittel benutzt zu haben.

München, 11.06.2018